


Article

Photocatalytic CO₂ Reduction to CH₄ and Dye Degradation Using Bismuth Oxychloride/Bismuth Oxyiodide/Graphitic Carbon Nitride (BiO_mCl_n/BiO_pI_q/g-C₃N₄) Nanocomposite with Enhanced Visible-Light Photocatalytic Activity

Yong-Ming Dai ¹, Wu-Tsan Wu ², Yu-Yun Lin ², Hsiao-Li Wu ², Szu-Han Chen ², Jih-Mirn Jehng ³ , Jia-Hao Lin ², Fu-Yu Liu ² and Chiing-Chang Chen ^{2,*} 

¹ Department of Chemical and Materials Engineering, National Chin-Yi University of Technology, Taichung 411, Taiwan

² Department of Science Education and Application, National Taichung University of Education, Taichung 403, Taiwan

³ Department of Chemical Engineering, National Chung Hsing University, Taichung 402, Taiwan

* Correspondence: ccchen@mail.ntcu.edu.tw; Tel.: +886-4-2218-3406; Fax: +886-4-2218-3560

Abstract: The use of visible-light-driven photocatalysts in wastewater treatment, photoreduction of CO₂, green solar fuels, and solar cells has elicited substantial research attention. Bismuth oxyhalide and its derivatives are a group of visible-light photocatalysts that can diminish electron-hole recombination in layered structures and boost photocatalytic activity. The energy bandgap of these photocatalysts lies in the range of visible light. A simple hydrothermal method was applied to fabricate a series of bismuth oxychloride/bismuth oxyiodide/grafted graphitic carbon nitride (BiO_mCl_n/BiO_pI_q/g-C₃N₄) sheets with different contents of g-C₃N₄. The fabricated sheets were characterized through XRD, TEM, SEM-EDS, XPS, UV-vis DRS, PL, and BET. The conversion efficiency of CO₂ reduction to CH₄ of BiO_mCl_n/BiO_pI_q of 4.09 μmol g⁻¹ can be increased to 39.43 μmol g⁻¹ by compositing with g-C₃N₄. It had an approximately 9.64 times improvement. The photodegradation rate constant for crystal violet (CV) dye of BiO_mCl_n/BiO_pI_q of *k* = 0.0684 can be increased to 0.2456 by compositing with g-C₃N₄. It had an approximately 3.6 times improvement. The electron paramagnetic resonance results and the quenching effects indicated that ¹O₂, •OH, h⁺, and •O₂⁻ were active species in the aforementioned photocatalytic degradation. Because of their heterojunction, the prepared ternary nanocomposites possessed the characteristics of a heterojunction of type II band alignment.

Keywords: composites; photocatalysis; BiO_mCl_n; BiO_pBr_q; g-C₃N₄; CO₂ reduction



Citation: Dai, Y.-M.; Wu, W.-T.; Lin, Y.-Y.; Wu, H.-L.; Chen, S.-H.; Jehng, J.-M.; Lin, J.-H.; Liu, F.-Y.; Chen, C.-C. Photocatalytic CO₂ Reduction to CH₄ and Dye Degradation Using Bismuth Oxychloride/Bismuth Oxyiodide/Graphitic Carbon Nitride (BiO_mCl_n/BiO_pI_q/g-C₃N₄) Nanocomposite with Enhanced Visible-Light Photocatalytic Activity. *Catalysts* **2023**, *13*, 522. <https://doi.org/10.3390/catal13030522>

Academic Editors: Juan José Rueda-Márquez, Javier Moreno-Andrés and Irina Levchuk

Received: 1 February 2023

Revised: 21 February 2023

Accepted: 1 March 2023

Published: 3 March 2023



Copyright: © 2023 by the authors. Licensee MDPI, Basel, Switzerland. This article is an open access article distributed under the terms and conditions of the Creative Commons Attribution (CC BY) license (<https://creativecommons.org/licenses/by/4.0/>).

1. Introduction

Semiconductor photocatalysis is an effective green technology because it can completely decompose environmental pollutants under mild conditions. The applications of semiconductor photocatalysts have elicited much scholarly attention for use in the treatment of organic pollutants because these photocatalysts can transform solar energy into chemical energy [1]. In addition, photocatalysts can also be used in the reduction of CO₂ and/or the construction of solar cells [2–6]. Since Fujishima and Honda reported the photocatalytic decomposition of water on the surface of TiO₂, TiO₂ has been widely studied to degrade pollutants or decompose water. However, the wide band gap (3.0–3.2 eV) of TiO₂ limits its application range [7]. Because the band gap in this range can only be applied to UV light with a small energy proportion in solar energy for photocatalysis, if the band gap can be reduced to below 2.5 eV, visible light can also be applied for photocatalysis, which accounts for a larger proportion of solar energy, and can be used more effectively.

Many semiconductor photocatalysts have been developed, including TiO₂, Fe₂O₃, CuO, and BiOX (X = I, Br, Cl). In particular, BiOX photocatalysts have drawn much research

interest due to their unique electronic structure [8–11]. Bismuth oxychloride (BiOCl) was first discovered in the early 19th century, and other bismuth oxyhalides (e.g., BiOF, BiOBr, and BiOI) have been discovered since then. BiOX crystals contain a layered structure of $[\text{Bi}_2\text{O}_2]^{2+}$, which results in them having highly asymmetric electrical, magnetic, and optical properties; thus, BiOX is frequently used in industrial chemicals, such as pharmaceuticals, pigments, and organic catalysts [12,13]. In BiOX crystals, four X and four O atoms surround each Bi atom to form a uniform asymmetric decahedral geometric structure [12]. $[\text{Bi}_2\text{O}_2]^{2+}$ has a strong covalent bond, which connects to the $[\text{X}]^-$ layer through the van der Waals force along the *c*-axis direction. Weak van der Waals forces and strong covalent bonds lead to the formation of layered structures. X_{np} ($n = 3, 4,$ and 5 corresponding to $X = \text{Cl}, \text{Br},$ and $\text{I},$ respectively) and O_{2p} occupy the top of the valence band of BiOX, and Bi_{6p} occupies the conduction band of BiOX [14]. Due to the unique atomic structure of BiOX, it has inherently superior photocatalytic properties. However, many bottlenecks must still be overcome to improve its performance in practical applications.

BiOX with the aforementioned compositions is a heterogeneous compound. There are heterojunctions between $\text{BiO}_m\text{Cl}_n/\text{BiO}_p\text{I}_q$ and $g\text{-C}_3\text{N}_4$. The first study to use $g\text{-C}_3\text{N}_4$ as a nonmetallic visible-light photocatalyst was published in 2008 [15]. However, because of the high electron–hole recombination rate of $g\text{-C}_3\text{N}_4$, its degradation efficiency is low; therefore, many studies have been conducted on composite photocatalysts containing $g\text{-C}_3\text{N}_4$ [16,17]. Studies have reported that heterojunctions associated with perovskite materials, including $\text{Bi}_2\text{SiO}_5\text{-}g\text{-C}_3\text{N}_4$ [18], $\text{SrFeO}_3\text{-}g\text{-C}_3\text{N}_4$ [19], $\text{BiOI-}g\text{-C}_3\text{N}_4$ [20], $\text{PbBiO}_2\text{Br/}g\text{-C}_3\text{N}_4$ [21], $\text{PbBiO}_2\text{I/Bi}_5\text{O}_7\text{I/}g\text{-C}_3\text{N}_4$ [22], and $\text{PbBiO}_2\text{Br/PbO/}g\text{-C}_3\text{N}_4$ [23], exhibit high photocatalytic activity.

When two or more different band gap photocatalysts are combined together, the heterojunction between their interfaces often has a synergistic effect on their photocatalysis. Many scholars have conducted a lot of research on this phenomenon in the past ten years. For example, Li et al. proposed the concept of a heterostructure of type II band alignment [22,24–26]. In addition, there are also newer descriptions of Z-scheme and S-scheme effects in the literature by Wang et al. [27], Xu et al. [28], and Wang et al. [29].

This study synthesized a $\text{BiO}_p\text{Cl}_g/\text{BiO}_x\text{I}_y$ compound and composited $\text{BiO}_p\text{Cl}_g/\text{BiO}_x\text{I}_y$ with $g\text{-C}_3\text{N}_4$ to separate photogenerated electron holes for achieving enhanced photocatalytic activity. The synthesized and composited photocatalyst materials were studied for the reduction of CO_2 to CH_4 and the degradation of CV dyes. At the same time, some discussions were made on the photocatalytic mechanism of prepared ternary nanocomposites.

2. Results and Discussion

2.1. Characterization of the Produced $\text{BiO}_m\text{Cl}_n/\text{BiO}_p\text{I}_q/g\text{-C}_3\text{N}_4$ Composites

The crystal phases of the 40 samples produced in this study were controlled by varying the sample synthesis ratio, solution pH, and reaction temperature. The hydrothermal time was 12 h; the molar ratio of Cl: I was 1:2 or 2:1; the solution pH was 1, 4, 7, 10, or 13; the reaction temperature was 100, 150, 200, or 250 °C. Table 1 presents the codes of the prepared samples.

2.1.1. XRD Analysis

XRD analysis was conducted to identify the compounds present in the synthesized samples. Each compound has a unique diffraction spectrum, and an analysis of the diffraction spectrum of a sample can indicate its composition.

Figure 1 shows that materials with different weight percentages of $g\text{-C}_3\text{N}_4$ (0, 2, 5, 10, 12, 15, 18, 20, and 55 wt%) were composited with the compound at a reaction temperature of 150 °C in 4 h. The synthesized samples were used to degrade CV dye to identify the catalyst with the highest degradation efficiency after electron–hole recombination. The XRD results of the BC1I2-250-4 sample agreed with those of $\text{Bi}_3\text{O}_4\text{Cl}$ (diffraction peaks at 2θ values of approximately 9.5°, 24.0°, 29.1°, 29.7°, 31.4°, 41.6°, and 45.2°), BiOCl (diffraction peaks at 2θ values of approximately 12.0°, 24.1°, 25.9°, 32.5°, 33.5°, 40.9°, 46.7°, 49.7°, 54.1°, 55.1°, and

58.6°), BiOI (diffraction peaks at 2θ values of approximately 9.7°, 29.7°, 31.7°, 45.5°, 51.3°, and 55.3°), Bi₄O₅I₂ (diffraction peaks at 2θ values of approximately 29.6°, 31.6°, 37.0°, 37.3°, 39.3°, 45.4°, 51.3°, and 55.1°), and Bi₄O₅Cl₂ (diffraction peaks at 2θ values of approximately 7.2°, 24.0°, 31.3°, 32.03°, 33.88°, 35.5°, 40.5°, and 41.1°). Thus, the aforementioned sample contains a crystalline phase comprising Bi₃O₄Cl, BiOI, BiOCl, Bi₄O₅Cl₂, and Bi₄O₅I₂. Pure g-C₃N₄ has a relatively strong diffraction peak at 27°. Small quantities of g-C₃N₄ were added into the samples, and the strength of the samples decreased with decreases in the weight percentage of the added g-C₃N₄. The aforementioned result verified the successful synthesis of heterogenous composite catalysts containing g-C₃N₄ in this study.

Table 1. Codes of the BiO_mCl_n/BiO_pI_q samples produced under various reaction temperatures, different pH values, two KCl:KI molar ratios, and a reaction time of 12 h.

Molar Ratio (Cl:I = 1:2)				
pH	Temperature (°C)			
	100	150	200	250
1	B1C1I2-1-100-12	B1C1I2-1-150-12	B1C1I2-1-200-12	B1C1I2-1-250-12
4	B1C1I2-4-100-12	B1C1I2-4-150-12	B1C1I2-4-200-12	B1C1I2-4-250-12
7	B1C1I2-7-100-12	B1C1I2-7-150-12	B1C1I2-7-200-12	B1C1I2-7-250-12
10	B1C1I2-10-100-12	B1C1I2-10-150-12	B1C1I2-10-200-12	B1C1I2-10-250-12
13	B1C1I2-13-100-12	B1C1I2-13-150-12	B1C1I2-13-200-12	B1C1I2-13-250-12

Molar Ratio (Cl:I = 2:1)				
pH	Temperature (°C)			
	100	150	200	250
1	B1C2I1-1-100-12	B1C2I1-1-150-12	B1C2I1-1-200-12	B1C2I1-1-250-12
4	B1C2I1-4-100-12	B1C2I1-4-150-12	B1C2I1-4-200-12	B1C2I1-4-250-12
7	B1C2I1-7-100-12	B1C2I1-7-150-12	B1C2I1-7-200-12	B1C2I1-7-250-12
10	B1C2I1-10-100-12	B1C2I1-10-150-12	B1C2I1-10-200-12	B1C2I1-10-250-12
13	B1C2I1-13-100-12	B1C2I1-13-150-12	B1C2I1-13-200-12	B1C2I1-13-250-12

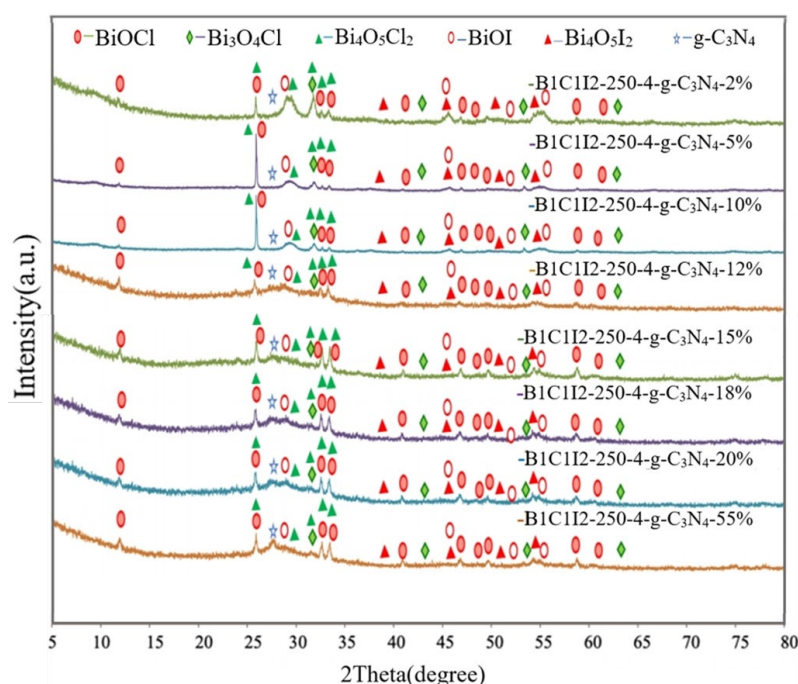


Figure 1. X-ray diffraction (XRD) patterns of the BiO_mCl_n/BiO_pI_q/g-C₃N₄ samples with g-C₃N₄ contents of 2%, 5%, 10%, 12%, 15%, 18%, 20%, and 55% that were prepared under a KCl:KI molar ratio of 1:2, a hydrothermal temperature of 250 °C, a pH of 4, and a reaction time of 12 h.

2.1.2. SEM and TEM

SEM and TEM mainly detect the morphology of samples. With the aid of their accessory equipment, functions such as detecting EDS, HR-TEM, and SAED can be added to determine the element composition and crystallinity of the sample. There are a lot of studies in the literature using SEM and TEM to detect the material properties of the bismuth oxyhalide photocatalyst [30–35]. With the different operating conditions for the synthesis of bismuth oxyhalide, the crystalline and morphology of the synthesized samples will also be different.

Figure 2a displays the bright-field TEM image of the BC1I2-4-250-g-C₃N₄-20% sample. The light part of this image represents g-C₃N₄ and the dark part of this image represents BiOCl and BiOI. The image analysis of the aforementioned composite indicated that BiO_mCl_n/BiO_pI_q was embedded in the sheet structure of g-C₃N₄. This phenomenon has similar results to BiOBr/g-C₃N₄ [34]. It showed that g-C₃N₄ coats other substances to become a wrinkled two-dimensional structure. When C₃N₄ belongs to an amorphous structure, it becomes difficult to see the state of encapsulation [33]. Figure 2b depicts the HR-TEM image of the aforementioned sample. TEM and XRD analyses indicate that BC1I2-250-4-g-C₃N₄-20% was mainly composed of BiOCl (d = 0.368 nm) and BiOI (d = 0.281 nm). The aforementioned result is the result of comparing the HR-TEM image and the JCPDS crystallization parameters of XRD. This is good evidence for the crystallization condition of the sample. Figure 2c presents the SAED pattern of this sample. The light spots were arranged in an aperture; therefore, the aforementioned sample was speculated to have a polycrystalline nature, and from the comparison of the pattern with XRD results, it can be proved that the samples in the figure correspond to BiOCl (110) and BiOI (002), respectively. Compared with the result of [34], the crystallinity of our sample is slightly inferior to [34]. Figure 2d illustrates the EDS results of BC1I2-4-250-g-C₃N₄-20%, with the ratio of each element being presented in the inset. The EDS results indicated that the aforementioned sample contained Bi, Cl, I, O, C, and N, which evinced the successful synthesis of BC1I2-4-250-g-C₃N₄-20%.

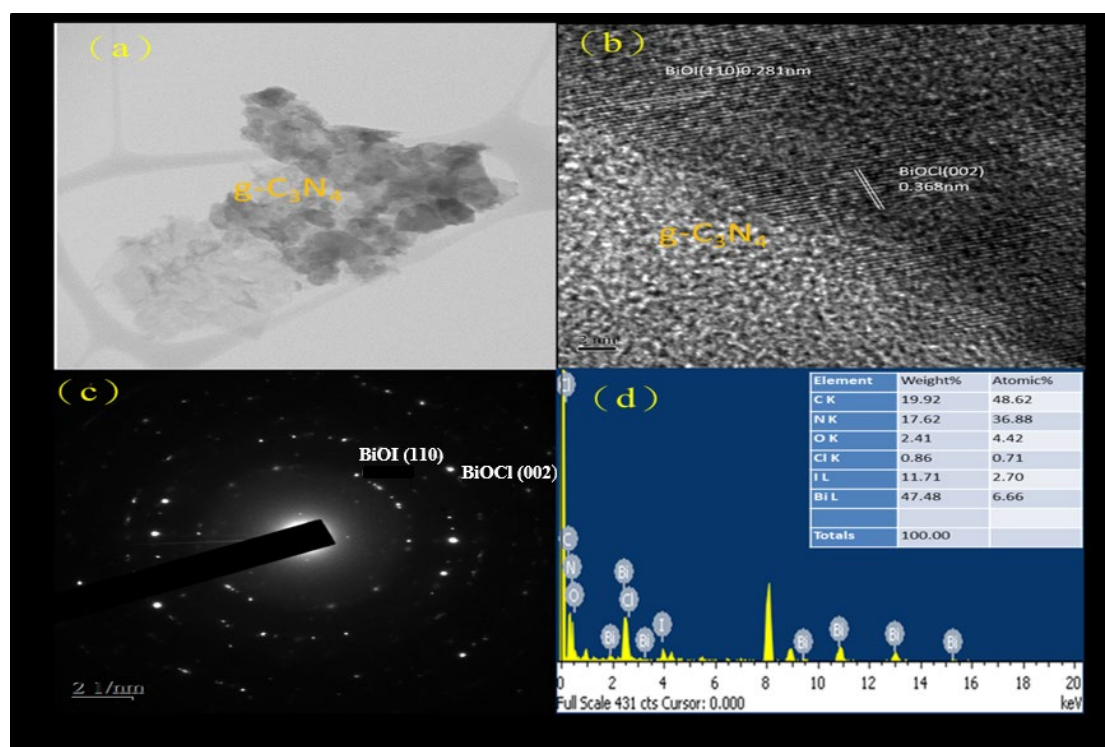


Figure 2. (a) FE-TEM image, (b) HR-TEM image, (c) SAD and (d) EDS of the BC1I2-250-4-g-C₃N₄-20% sample prepared using the hydrothermal autoclave method.

2.1.3. Analysis of XPS Spectra

In XPS, X-rays are used to excite electrons in the inner shells of atoms for quantitatively analyzing the electronic and chemical states of the elements in a material. Therefore, this method is also called electron spectroscopy for chemical analysis (ESCA). The electronic transition state in the principal quantum orbital can be quantitatively analyzed using XPS, and the electronic transition state in the angular quantum orbital can be examined through the deconvolution of the XPS spectrum. XPS also indicates whether the bonding energy of a substance has changed. An X-ray photoelectron spectrometer can be used to analyze the valence state and configuration of a sample. Moreover, the elemental composition of a sample can be determined from its XPS spectrum. Figure 3a displays the complete XPS spectra of BC1I2-250-4 and BC1I2-250-4-g-C₃N₄-20%. As depicted in the aforementioned figure, the photoelectrons used in XPS excited the I 3p, Bi 4p, I 3d, O 1s, Bi 4f, Bi 4d, N 1s, C 1s, Cl 2p, Bi 4f, I 4d, O 2s, and Bi 5d energy levels of the aforementioned samples. Our lab has performed XPS analysis on BiO_xCl_y/BiO_mBr_n/g-C₃N₄ and determined its XPS pattern [31].

Figure 3b displays the Bi 4f diagram of BC1I2-250-4 and BC1I2-250-4-g-C₃N₄-20%. In this figure, peaks representing Bi³⁺ were located at 158.3 and 163.6 eV and the characteristic peak positions representing Bi^{+3-x} were located at 155.9 and 161.3 eV. By contrast, Bi^{+3-x} peaks were not observed in [31]. Subtle differences existed in the bonding electronic configurations of Bi in BiO_mCl_n/BiO_pI_q and BiO_xCl_y/BiO_mBr_n. However, the same trend was observed in the right displacement caused by the addition of g-C₃N₄ for both aforementioned composites. The aforementioned result was obtained because when Bi was partially synthesized with the iodine element using a high-pressure hydrothermal method, it would be reduced to a low valence state that corresponds to the signals of the 4d_{3/2}, 4d_{5/2}, 4f_{5/2}, 4f_{7/2}, and 5d states. Figure 3c shows the O1s peaks of BC1I2-250-4 and BC1I2-250-4-g-C₃N₄-20%. The full-width at half-maximum (FWHM) of Bi⁺³-O was 0.9863–1.1920 eV, and the FWHM of Bi^{+3-x}-O was 1.7639–2.6427 eV. The BiO_xCl_y/BiO_mBr_n spectrum obtained in [31] contained only a single peak, whereas the BiO_mCl_n/BiO_pI_q spectrum obtained in this study contained two peaks. This observation was probably because the splitting of Bi into two valence states, namely Bi⁺³ and Bi^{+3-x}, results in the splitting of O into two valence states. Figure 3d presents the N1s diagram of g-C₃N₄ and BC1I2-250-4-g-C₃N₄-20%. The FWHM of C=NC was 1.1464–1.1773 eV, and the FWHM of N-(C)₃ and HN-(C)₂ was 1.9754–2.133 eV. These results are consistent with those obtained in [31]. Thus, both BiO_mCl_n/BiO_pI_q and BiO_xCl_y/BiO_mBr_n can be composited with g-C₃N₄. Figure 3e displays the Cl 2p narrow spectrum of BC1I2-250-4 and BC1I2-250-4-g-C₃N₄-20%, whose Cl 2p peaks were located at 196.8 and 198.7 eV, respectively, which corresponded to 2p_{3/2} and 2p_{1/2}. The aforementioned peaks are the characteristic peaks of Cl, which agrees with the results of [31]. Figure 3f illustrates the C 1s narrow spectra of BC1I2-250-4-g-C₃N₄-20% and g-C₃N₄. The C1s spectrum of BC1I2-250-4-g-C₃N₄-20% exhibited two peaks that corresponded to binding energies of approximately 284.4 and 287.8 eV. This result agrees with that in [31]. As displayed in Figure 3g, the binding energy of the characteristic positions of I was 617.8–629.7 eV, with the binding energies of 617.8 and 629.7 eV corresponding to I3d_{5/2} and I3d_{3/2}. This result is in line with those obtained in previous studies for the BiO_xI_y [36] and BiO_xCl_y/BiO_mBr_n/BiO_pI_q [32] composites. A system containing I in the form of PbBiO₂I/Bi₅O₇I/g-C₃N₄ has a complex but consistent peak distribution in [22].

2.1.4. UV-Vis DRS Analysis

The energy bandgaps (*E_g*) of the samples were calculated from the data obtained using UV-vis DRS and the Tauc plot method [14,37]. Some of the results and discussion of this work are shown in the Supplementary Materials. All *E_g* were in the visible light range (400 nm < λ < 700 nm, or 1.77 eV < *E_g* < 3.1 eV). Therefore, it can be expected that the photocatalysts of this work are promising to utilize most of the energy of sunlight for photocatalysis.

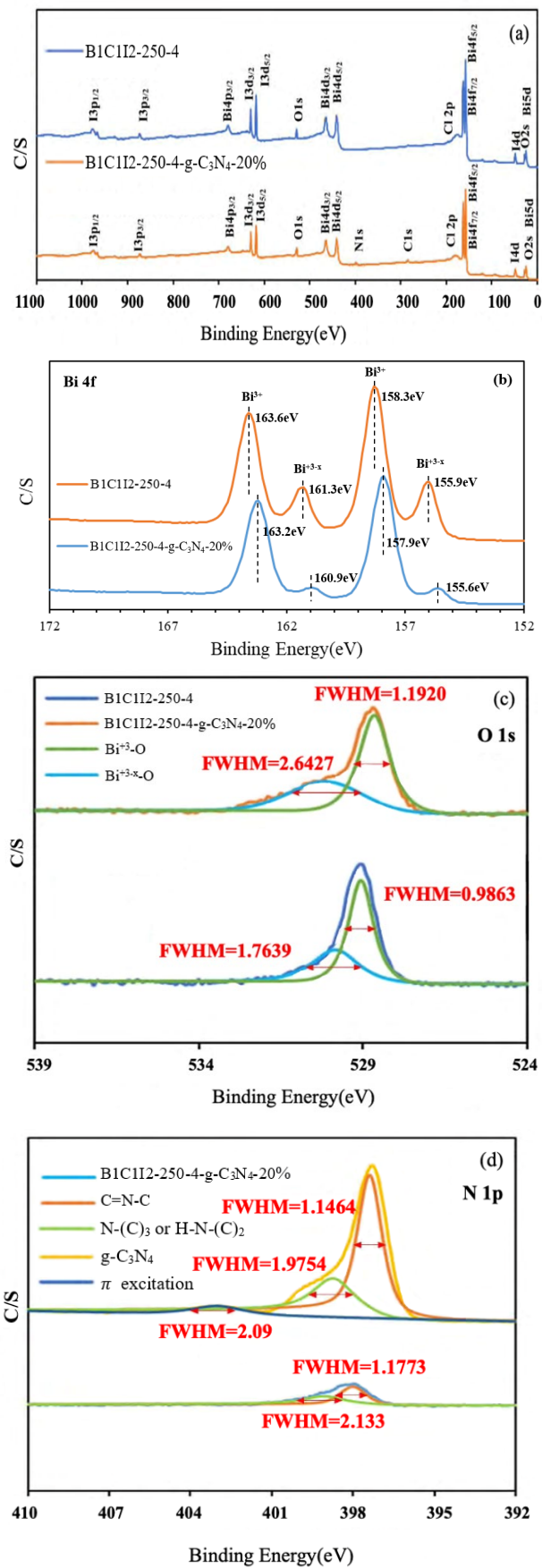


Figure 3. Cont.

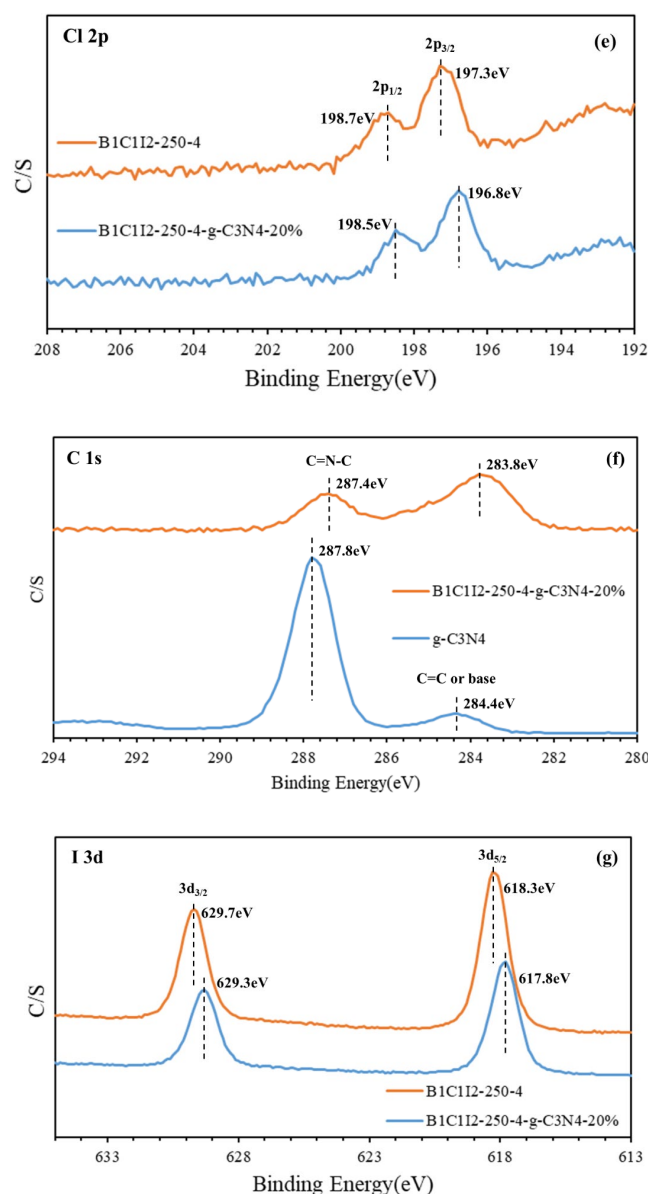


Figure 3. High-resolution X-ray photoelectron spectroscopy spectra of the BiO_mCl_n/BiO_pI_q/g-C₃N₄-20% photocatalyst prepared under a KCl:KI molar ratio of 1:2, a hydrothermal temperature of 250 °C, a pH of 4: (a) complete survey, (b) Bi-4f, (c) O-1s, (d) N-1s, (e) Cl-2p, (f) C-1s, and (g) I-3d spectra.

Figure 4 displays the UV–vis spectra of BiO_mCl_n/BiO_pI_q/g-C₃N₄ samples with 2%, 5%, 10%, 12%, 15%, 18%, 20%, and 100% g-C₃N₄ under a pH of 4 and a hydrothermal temperature of 250 °C. The aforementioned figure indicates that the sample color changed from orange to yellow as the g-C₃N₄ content in the samples increased; specifically, with such an increase from 0% to 10%, the absorption peak of the sample moved to the left and deviated from the visible light region. However, when the content of g-C₃N₄ increased to 20%, the absorption peak moved to the right. Thus, the addition of g-C₃N₄ considerably affected the absorption peaks in the DRS spectra. Similar results were observed in [6] for BC1B1I1 when graphene oxide was added to it. The formation of a heterojunction by using two photocatalysts in different ratios considerably affects the energy bandgap of a material. The E_g values of B1C1I2-250-4-g-C₃N₄-15%, B1C1I2-250-4-g-C₃N₄-18%, and B1C1I2-250-4-g-C₃N₄-20% (2.03, 1.89, and 2.01 eV, respectively) were less than that of g-C₃N₄ (2.71 eV). This result indicates that the prepared photocatalysts containing g-C₃N₄ can absorb more visible light than can pure g-C₃N₄.

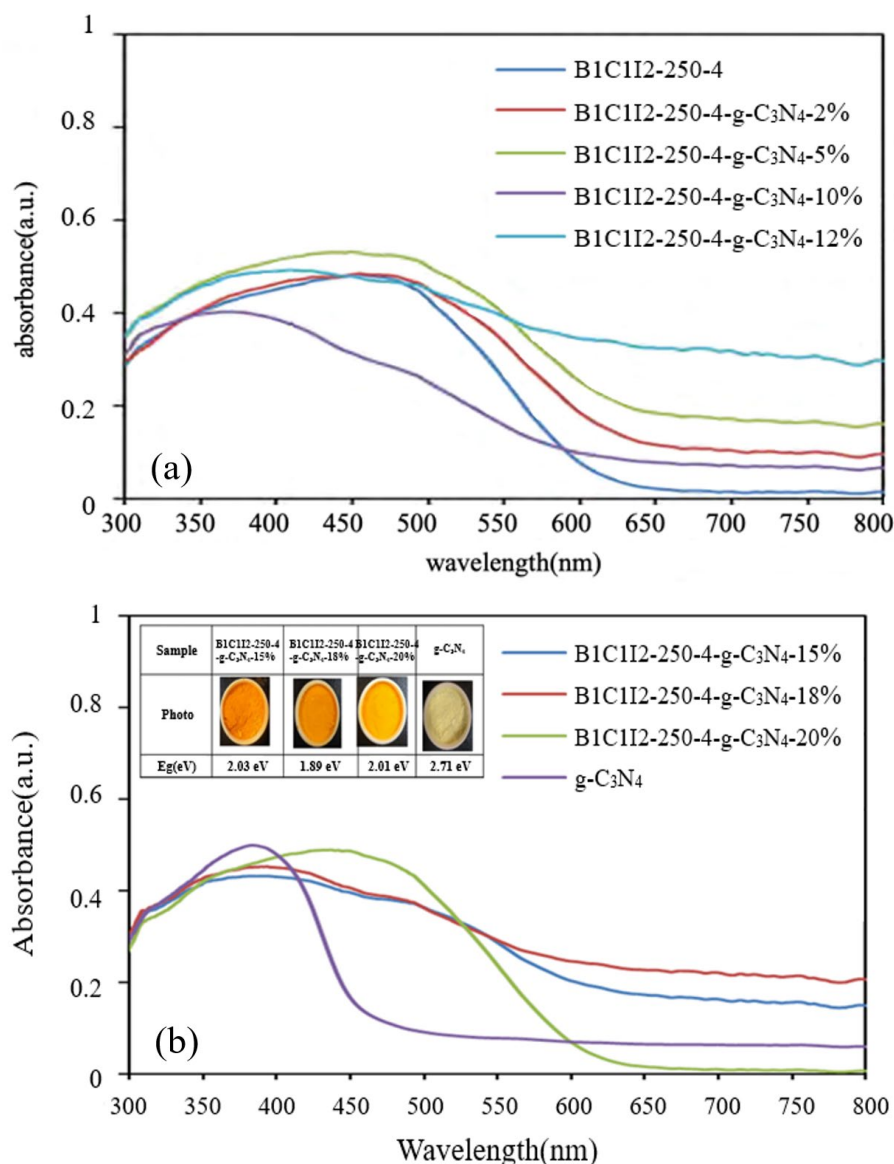


Figure 4. UV-vis absorption spectra of BiOmcIn/BiOpIq/g-C₃N₄ photocatalysts with different g-C₃N₄ contents that were prepared under a KCl:KI molar ratio of 1:2, a hydrothermal temperature of 250 °C, and a pH of 4: (a) photocatalysts with g-C₃N₄ contents of 2%, 5%, 10%, and 12%; (b) photocatalysts with g-C₃N₄ contents of 15%, 18%, and 20%.

2.1.5. PL Analysis

We used a photo-excited fluorescence spectrometer (PL) to determine the electron-hole recombination rate of the samples because the hydroxyl radicals and oxygen radicals required for photocatalysis originated from the reduction and oxidation of electrons and holes in the photocatalysts. When the electron-hole recombination rate is excessively high, the generation rates of hydroxyl radicals and superoxide radicals affect the photocatalytic efficiency [38]. Therefore, the photocatalytic efficiency can be determined from the results of PL spectroscopy. As displayed in Figure 5, the electron-hole recombination rates of the uncomposed samples were lower than those of the composed samples. The scanning range of the spectrum was 350–600 nm, and the excitation wavelength of 300 nm was used. The electron-hole recombination rate of pure g-C₃N₄ was higher than those of all the uncomposed samples, and BC1I2-250-4-g-C₃N₄-20% had a lower electron-hole recombination rate than pure g-C₃N₄ did.

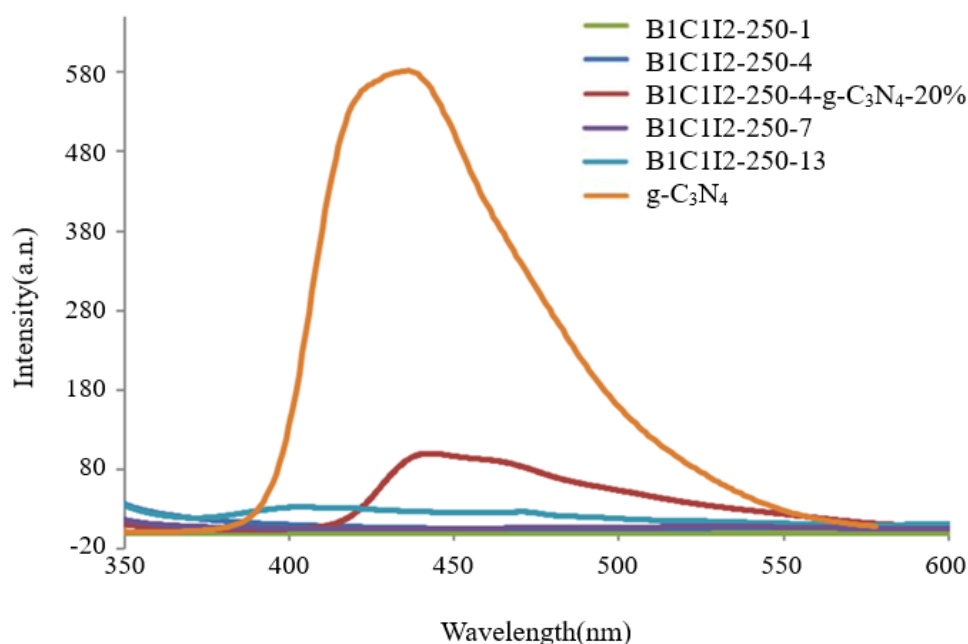


Figure 5. Photoluminescence spectra of the BiO_mCl_n/BiOpIq/g-C₃N₄–20% photocatalyst prepared under a KCl:KI molar ratio of 1:2, a hydrothermal temperature of 250 °C, and a pH of 4.

Pure g-C₃N₄ exhibited the highest electron–hole recombination rate in this study. Therefore, when electrons and holes were generated in pure g-C₃N₄ through photocatalysis, they recombined quickly. Consequently, free radicals that react with CV could not form. However, low electron–hole recombination rates were observed in samples with 0 wt% g-C₃N₄ (i.e., C1I2-250-1, C1I2-250-4, C1I2-250-7, and C1I2-250-13). The aforementioned result can be attributed to two possibilities: (1) the generated electrons and holes formed free radicals to react with CV, so the recombination of electron holes was very weak; (2) the generated electrons and holes were few in number; therefore, there was no recombination of electrons and holes.

The CV photodegradation efficiency of the samples with 20 wt% g-C₃N₄ was greater than that of the sample with pure g-C₃N₄ and those of the B1C1I2-250-1, B1C1I2-250-4, B1C1I2-250-7, and B1C1I2-250-13 samples because the numbers of electrons and holes generated through photocatalysis and the electron–hole recombination rate were higher in the samples with 20 wt% g-C₃N₄, which reached the better and more appropriate state.

2.1.6. BET Analysis

The nitrogen gas content in and nitrogen adsorption–desorption isotherm of the BiO_mCl_n/BiOpIq/g-C₃N₄–20% sample were used to calculate its pore volume and BET-specific surface area, respectively. As the BET-specific surface area increased, the reaction area on the sample surface increased, which affected the reaction rate. As displayed in Figure 6, the nitrogen adsorption–desorption isotherm of the aforementioned sample was a type IV isotherm with an H3 hysteresis loop [39–42] (as defined by the International Union of Pure and Applied Chemistry). The hysteresis loop of this isotherm ($P/P_0 > 0.8$) indicates that the aforementioned sample contained mesopores (size = 2–50 nm) and macropores (size ≥ 50 nm). Using the Barrett–Joyner–Halenda method, we computed the BET-specific surface area to be 17.4356 m²/g and the average pore size to be 27.76 nm. [43]

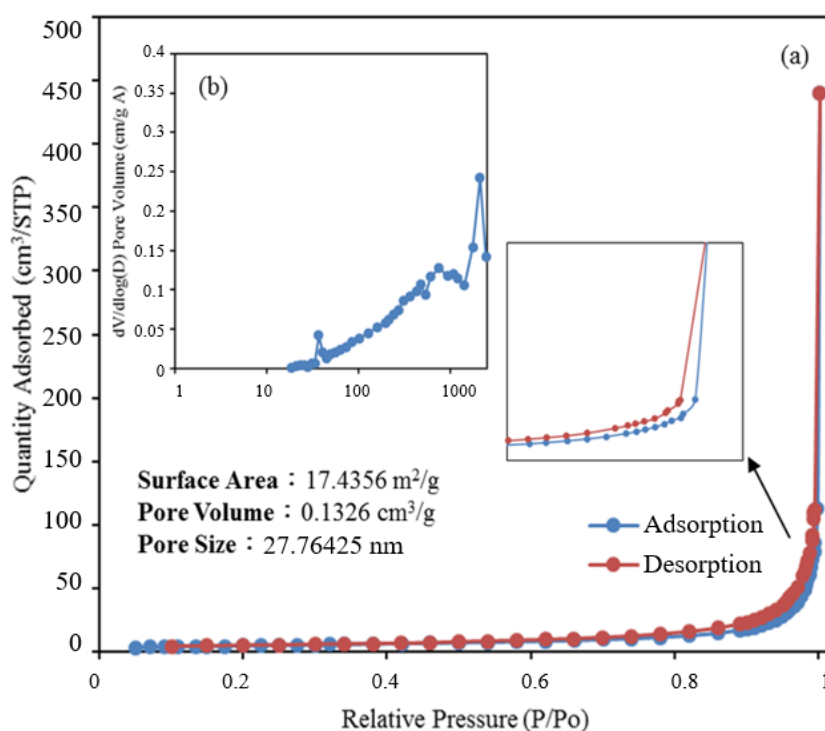


Figure 6. (a) Nitrogen adsorption–desorption isotherms and (b) the corresponding pore-size distribution curve (inset) for BiOmCln/BiOpIq/g-C₃N₄–20% photocatalyst prepared under a KCl:KI molar ratio of 1:2, a hydrothermal temperature of 250 °C, and a pH of 4.

Samples with appropriate pore sizes and a large specific surface area contain numerous surface activation sites, which promote product and reactant transfer. An appropriate pore size and large specific surface area can result in high electron–hole separation and a high photoenergy yield, which result in improved photocatalysis.

2.2. Photocatalytic Activity

2.2.1. Photocatalytic Reduction of CO₂

The application of semiconductor photocatalysts in carbon dioxide reduction, water splitting, and nitrogen fixation is an important topic at present. The mechanism for the above applications is that semiconductor photocatalysts have a tunable solar absorption range to support photo-excited electrons to reach feasible reduction potentials for the above applications [44–46]. Despite various strategies including the semiconductor heterojunction, heteroatom doping, defect engineering, new semiconductor synthesis, and morphology control that have been used to improve the segregation performance of photogenerated charges, the photocatalytic design to achieve efficient reduction, splitting, and fixation of extremely stable CO₂, H₂O, and N₂ is still very challenging [47–49]. Generally, it is very difficult for a single catalyst to generate a sufficient number of photogenerated electrons or active species for CO₂ conversion, so the photocatalytic CO₂ reduction efficiency of the single catalyst is generally poor. Furthermore, it is also a challenge to utilize visible light or solar radiation and achieve efficient charge separation and robust redox capabilities [50,51].

Figure 7 shows the results of CO₂ reduction by B1C1I2, B1C1I2/g-C₃N₄, and g-C₃N₄. This result shows that the CO₂–CH₄ conversion efficiency of the composite B1C1I2/g-C₃N₄ was much better than those of the individual B1C1I2 and g-C₃N₄. The conversion efficiency of CO₂ reduction to CH₄ of BiO_mCl_n/BiO_pI_q of 4.09 μmol g^{−1}h^{−1} can be increased to 39.43 μmol g^{−1} by compositing with g-C₃N₄. It had an approximately 9.64 times improvement.

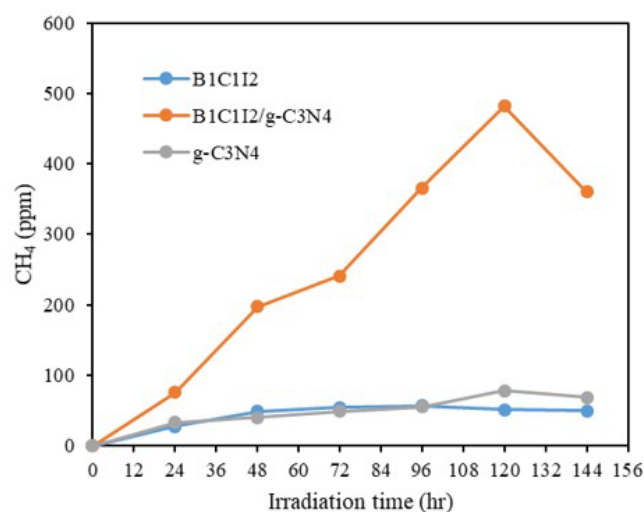


Figure 7. Photocatalytic reduction of CO₂ as a function of irradiation time over B1C1I2, B1C1I2/g-C₃N₄, and g-C₃N₄.

2.2.2. Photocatalytic Degradation of CV

The photocatalytic effects of photocatalysts are key to the degradation of organic pollutants. In this study, CV dye was degraded using the prepared samples under different conditions to investigate their photocatalytic degradation effects. Moreover, the sample with the best photocatalytic degradation effect was identified. As displayed in Figure 8, the signal intensity of CV at 591 nm gradually weakened when it was degraded by using the prepared samples; thus, CV was successfully degraded by these samples. The original maximum absorption peak of CV dye was at 591 nm; however, the spectrum of this dye exhibited a hypsochromic shift as the irradiation time increased. CV may have undergone a structural change, which also indicates that this dye was successfully degraded by the prepared photocatalyst samples [52,53]. Jiang et al. [54] and Liao et al. [55] detailed the mechanism underlying the photocatalytic degradation of CV under visible-light irradiation. The aforementioned authors have indicated that photocatalysis enables CV dyes to form N-demethylated intermediates. Moreover, the conjugated chromophores of CV dyes can be cleaved through BiO_mCl_n/BiO_pI_q/g-C₃N₄ photocatalysis [53].

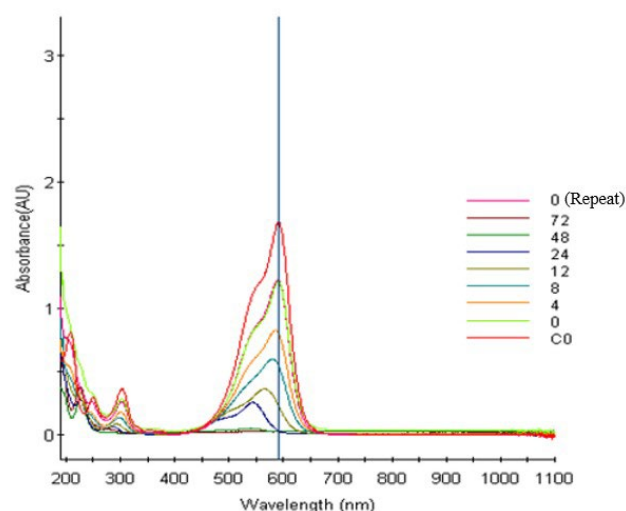


Figure 8. Temporal variations in the UV-vis adsorption of the aqueous BiO_mCl_n/BiO_pI_q/g-C₃N₄-20% photocatalyst prepared under a KCl:KI molar ratio of 1:2, a hydrothermal temperature of 250 °C, and a pH of 4 during the photocatalytic degradation of CV on the photocatalyst under visible-light irradiation.

Figure 9 presents the CV degradation efficiency diagram of $\text{BiO}_m\text{Cl}_n/\text{BiO}_p\text{I}_q$ for a Cl:I ratio of 1:2, a hydrothermal temperature of 250 °C, and different pH values. The degraded pollutant in this study was 100 mL of 10 ppm of CV dye. By using relevant first-order kinetic equations ($(dC_t/dt) = kC_t$ and $\ln(C_0/C_t) = kt$, where C_t is concentration of the CV dye at time t and k is the reaction rate constant), we determined the k and R^2 values for different pH values. Specifically, for the pH values of 1, 4, 7, 10, and 13, the k values were 0.017, 0.068, 0.035, 0.033, and 0.015 h^{-1} , respectively, and the R^2 values were above 0.90 (Table 2), $\text{BiO}_m\text{Cl}_n/\text{BiO}_p\text{I}_q$ had a superior photocatalytic degradation effect at a pH of 4. It was also found from the literature that under similar synthesis conditions, a Cl: I (or Br) ratio of 1:2, a hydrothermal temperature of 250 °C, and pH = 4, BiO_pI_q (BC1I2-250-4, $k = 0.068 \text{ h}^{-1}$) gave slightly better results than for $\text{BiO}_x\text{Cl}_y/\text{BiO}_m\text{Br}_n$ (BC1B2-250-4, $k = 0.043 \text{ h}^{-1}$) [31].

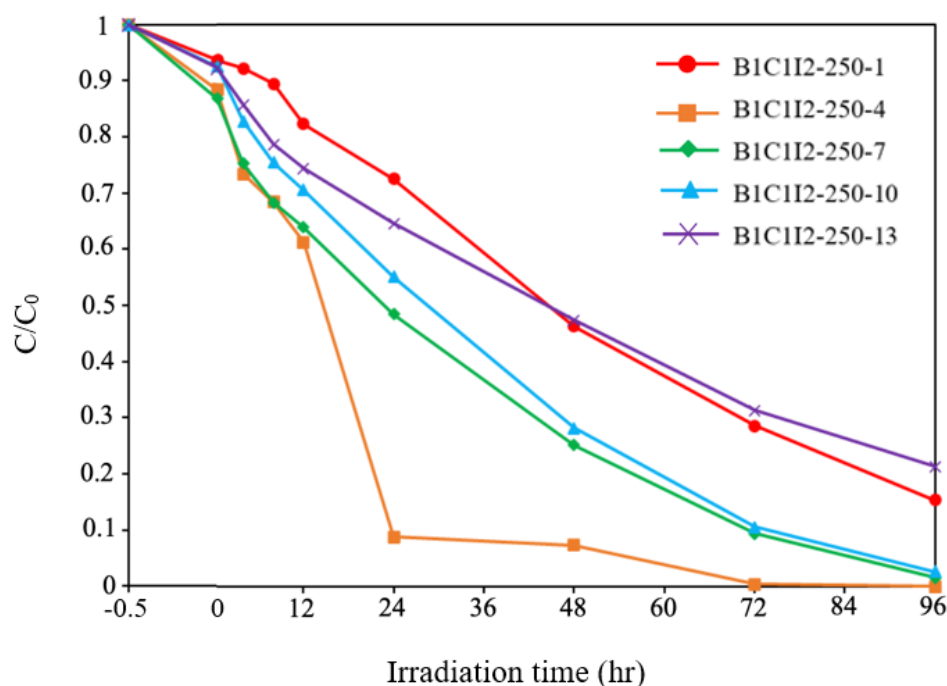


Figure 9. Photodegradation of CV with the irradiation time on various $\text{BiO}_m\text{Cl}_n/\text{BiO}_p\text{I}_q$ photocatalysts prepared under a KCl:KI molar ratio of 1:2, a pH of 1–13, and a hydrothermal temperature of 250 °C.

Table 2. Rate constants for the pseudo-first-order degradation of CV on the prepared $\text{BiO}_m\text{Cl}_n/\text{BiO}_p\text{I}_q$ photocatalysts under visible-light irradiation.

Cl I = 1 2										
Temperature (°C)	pH									
	1		4		7		10		13	
	k (h^{-1})	R^2	k (h^{-1})	R^2	k (h^{-1})	R^2	k (h^{-1})	R^2	k (h^{-1})	R^2
100	0.01	0.974	0.034	0.982	0.027	0.986	0.043	0.977	0.008	0.903
150	0.021	0.939	0.036	0.977	0.026	0.986	0.025	0.974	0.008	0.903
200	0.005	0.812	0.033	0.984	0.031	0.979	0.035	0.986	0.013	0.994
250	0.017	0.973	0.068	0.983	0.035	0.945	0.033	0.961	0.015	0.997

Figure 10 displays the degradation efficiency graph of the $\text{BiO}_m\text{Cl}_n/\text{BiO}_p\text{I}_q/\text{g-C}_3\text{N}_4$ samples with $\text{g-C}_3\text{N}_4$ contents of 20%, 40%, 60%, and 80% for a Cl:I ratio of 1:2, a pH of 4, and a reaction temperature of 250 °C. To ensure that the CV dye was completely adsorbed by the prepared catalysts, the first 30 min of the degradation reaction was conducted in a dark room. Figure 10 indicates that C1I2-250-4- $\text{g-C}_3\text{N}_4$ -20% had a superior photocatalytic effect on the other adopted samples. By using relevant first-order kinetic

equations $(dC_t/dt) = -kC_t$ and $\ln(C_0/C_t) = kt$, we determined the k and R^2 values for different $g\text{-C}_3\text{N}_4$ contents. For $g\text{-C}_3\text{N}_4$ contents of 20%, 40%, 60%, and 80%, the k values were determined to be 0.2456, 0.1943, 0.1041, and 0.0584 h^{-1} , respectively, and the R^2 values were determined to be above 0.9. Compared with the results of $\text{BiO}_x\text{Cl}_y/\text{BiO}_m\text{Br}_n/g\text{-C}_3\text{N}_4$ ($k = 0.0282\text{--}0.0710\text{ h}^{-1}$) [4], the results of $\text{BiO}_m\text{Cl}_n/\text{BiO}_p\text{I}_q/g\text{-C}_3\text{N}_4$ were much better.

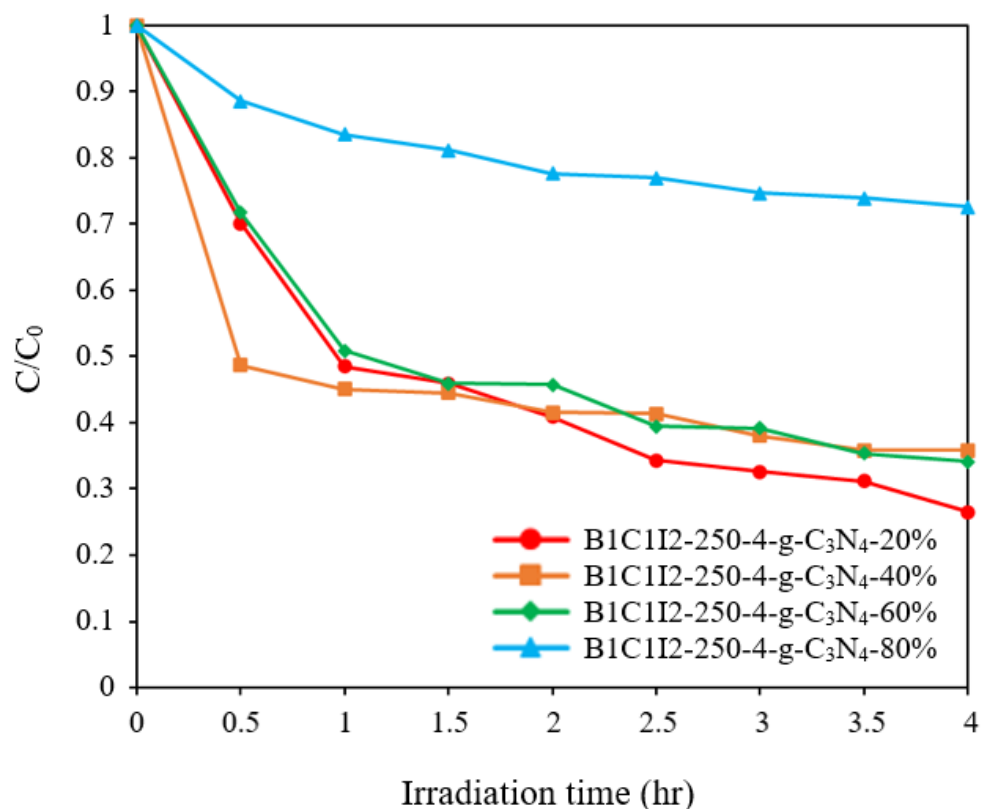


Figure 10. Photodegradation of CV with the irradiation time on $\text{BiO}_m\text{Cl}_n/\text{BiO}_p\text{I}_q/g\text{-C}_3\text{N}_4$ samples with $g\text{-C}_3\text{N}_4$ contents of 20–80% that were prepared under a KCl:KI molar ratio of 1:2, a pH of 4, and a hydrothermal temperature of $250\text{ }^\circ\text{C}$.

The aforementioned results were in line with the PL results. When the proportion of $g\text{-C}_3\text{N}_4$ was 20%, optimal numbers of electrons and holes were generated through photocatalysis and an optimal electron–hole recombination rate was achieved. The photocatalytic efficiency at a $g\text{-C}_3\text{N}_4$ content of 80% was considerably lower than that at a $g\text{-C}_3\text{N}_4$ content of 20% (Figure 10). The reason can be inferred from the mechanism that when the content of $g\text{-C}_3\text{N}_4$ increased from 0.5% to 20%, the generation of $\bullet\text{OH}$ increased. However, when the content of $g\text{-C}_3\text{N}_4$ was further increased to 80%, the formation of $\bullet\text{OH}$ decreased. Equations (1) and (2) describe photocatalytic CV degradation by active substances over multiple cycles.

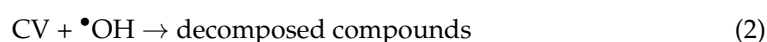
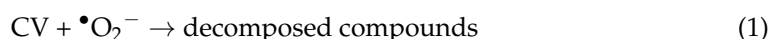


Table 3 presents a summary of the results of all the irradiation experiments. Among the samples without $g\text{-C}_3\text{N}_4$, the BC2I1-100-4, BC1I2-250-4, and BC2I1-150-4 samples had the top three degradation efficiencies. Among all the samples, the C1I2-250-4- $g\text{-C}_3\text{N}_4$ -20% sample had the highest degradation efficiency. The degradation efficiency of this sample exceeded that of the uncomposited C2I1-100-4 sample by more than three times.

Table 3. Rate constants for the pseudo-first-order degradation of CV on the prepared $\text{BiO}_m\text{Cl}_n/\text{BiO}_p\text{I}_q/\text{g-C}_3\text{N}_4$ samples under visible-light irradiation.

Photocatalyst	k (h^{-1})	R^2
BC2I1-100-4-g-C3N420%	0.0208	0.8935
BC2I1-100-4-g-C3N440%	0.0349	0.92
BC2I1-100-4-g-C3N460%	0.0244	0.9958
BC2I1-100-4-g-C3N480%	0.0331	0.9843
g-C3N4	0.0162	0.9027
BC1I2-250-4-g-C3N420%	0.2456	0.9732
BC1I2-250-4-g-C3N440%	0.1041	0.9767
BC1I2-250-4-g-C3N460%	0.1943	0.9938
BC1I2-250-4-g-C3N480%	0.0584	0.9887
BC2I1-150-4-g-C3N420%	0.0125	0.9027
BC2I1-150-4-g-C3N440%	0.0349	0.8125
BC2I1-150-4-g-C3N460%	0.0244	0.9841
BC2I1-150-4-g-C3N480%	0.0347	0.9786
BC1I2-250-4-g-C3N40.5%	0.0868	0.9859
BC1I2-250-4-g-C3N41%	0.1962	0.9421
BC1I2-250-4-g-C3N42%	0.1656	0.9896
BC1I2-250-4-g-C3N45%	0.0514	0.9849
BC1I2-250-4-g-C3N410%	0.0373	0.9339
BC1I2-250-4-g-C3N412%	0.0462	0.9811
BC1I2-250-4-g-C3N415%	0.0474	0.9565
BC1I2-250-4-g-C3N418%	0.0399	0.944
BC1I2-250-4-g-C3N425%	0.0492	0.9346
BC1I2-250-4-g-C3N430%	0.0462	0.9811

We used fluorescent lamps with very weak light intensity to conduct experiments, which can prove that the new composite material produced by bismuth oxyhalide photocatalyst composite $\text{g-C}_3\text{N}_4$ can still exert the photodegradation effect under weak visible-light sources. (More “Photocatalytic degradation of CV” can be found in the Supplementary Materials).

2.2.3. Reuse of $\text{BiOCl}/\text{BiOI}/\text{g-C}_3\text{N}_4$

Reuse rate tests were conducted to determine the reuse rate and stability of the prepared catalysts. Each of the prepared photocatalysts was used to photodegrade 10 ppm of CV dye five times. Subsequently, we recovered the remaining catalyst, filtered it with distilled water, and dried it for 24 h in an oven. Figure 11a displays the reuse efficiency of the $\text{BiO}_m\text{Cl}_n/\text{BiO}_p\text{I}_q/\text{g-C}_3\text{N}_4$ catalyst with 20% $\text{g-C}_3\text{N}_4$ for the degradation of CV dye under a Cl:I ratio of 1:2, a pH of 4, and a hydrothermal temperature of 250 °C. The degradation efficiency of the aforementioned catalyst remained above 90.5% even after it was used three times for photodegradation; thus, this catalyst can be reused. The aforementioned result is similar to a result obtained in [52]. Figure 11b presents the XRD patterns of BC1I2-4-250-g-C₃N₄-20% before use and after five times of use. The aforementioned catalyst exhibited a similar crystal phase after five times of use, which indicates that this catalyst had satisfactory stability.

In terms of practicality, a re-usability of only three times represents that the stability of the material needs to be strengthened. However, from the perspective of innovative research, this does not deny the fact that the experiment is reproducible. There are some studies in the literature that used various surface modification or doping trace element methods to improve the stability of photocatalysts. The primary goal of this experiment was to confirm the reproducibility of this innovative photocatalyst. Its stability may be related to the bonding strength between the crystalline elements of its material, or it may also be related to its own crystalline stability. How to strengthen the stability of this innovative photocatalyst and improve its feasibility in practical application can be listed as a project for future work.

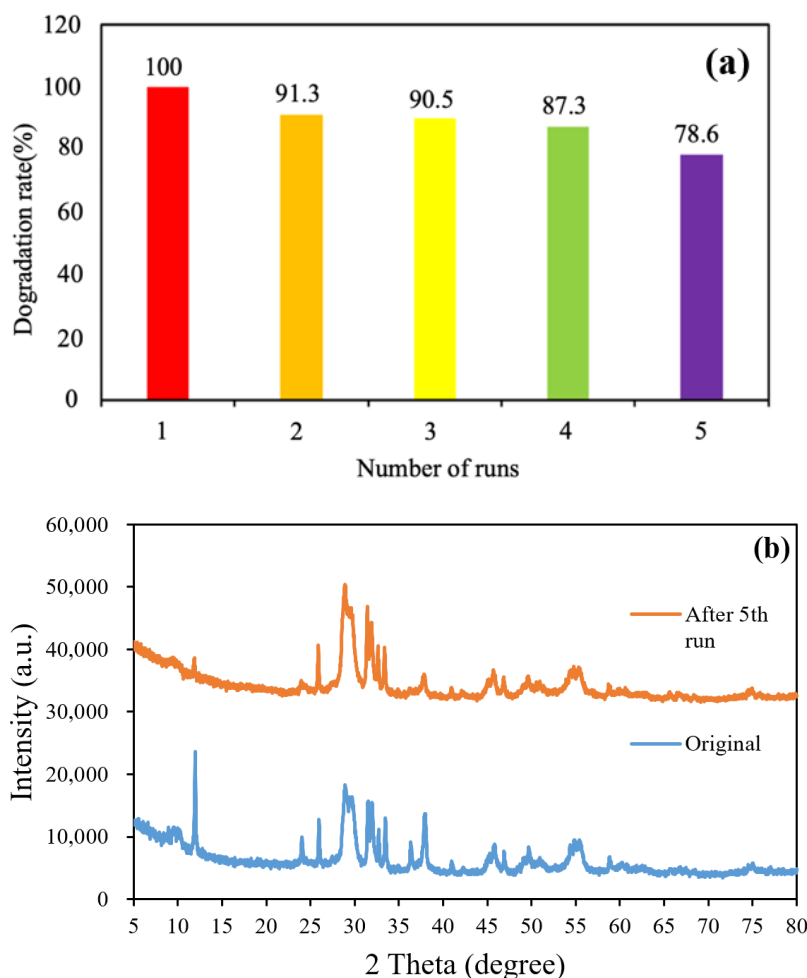


Figure 11. (a) Cycling runs in the photocatalytic degradation of CV in the presence of the BiOmcIn/BiOpIq/g-C₃N₄-20% photocatalyst prepared under a KCl:KI molar ratio of 1:2, a hydrothermal temperature of 250 °C, and a pH of 4. (b) XRD patterns of the aforementioned photocatalyst before use and after five times of use.

2.2.4. Verification of Active Species and EPR Analysis

Scavengers can be used to confirm the presence of main free radicals produced by catalysts during photocatalytic reactions. Different photocatalytic effects may occur when different radical scavengers are added during the photodegradation reaction. Studies have demonstrated that the main free radicals generated by the synthesized catalysts are trapped free radicals [56,57]. In this study, an experiment was conducted in which IPA, BQ, SA, and AO were used as the scavengers of hydroxyl radicals ($\bullet\text{OH}$), superoxide radicals ($\bullet\text{O}_2^-$), singlet oxygen ($^1\text{O}_2$), and holes (h^+), respectively. Figure 12a displays the variations in the dye concentration changes for the BC1I2-250-4-g-C₃N₄-20% photocatalyst when different capture agents were used. In this figure, the Y-axis ($1-\eta$) represents $(\Delta C_0 - \Delta C_s)/\Delta C_0 \times 100\%$, where ΔC_0 is the CV concentration change without scavenger illumination for 96 h, and ΔC_s is the CV concentration change with scavenger illumination for 96 h. The higher the $(1-\eta)$, the more obvious the change in the CV degradation rate. This meant that the specified active species was captured obviously by the corresponding scavenger. This implied that the specified active species plays an increasingly important role in the photodegradation of CV solution. The proportions of BQ and AO in the aforementioned photocatalysts were 23.5% and 13.2%, respectively. Thus, the main active species produced by the photodegradation reaction of BC1I2-250-4-g-C₃N₄-20% was the $\bullet\text{O}_2^-$ superoxide radical; however, the h^+ , $\bullet\text{OH}$, and $^1\text{O}_2$ species also exerted an influence.

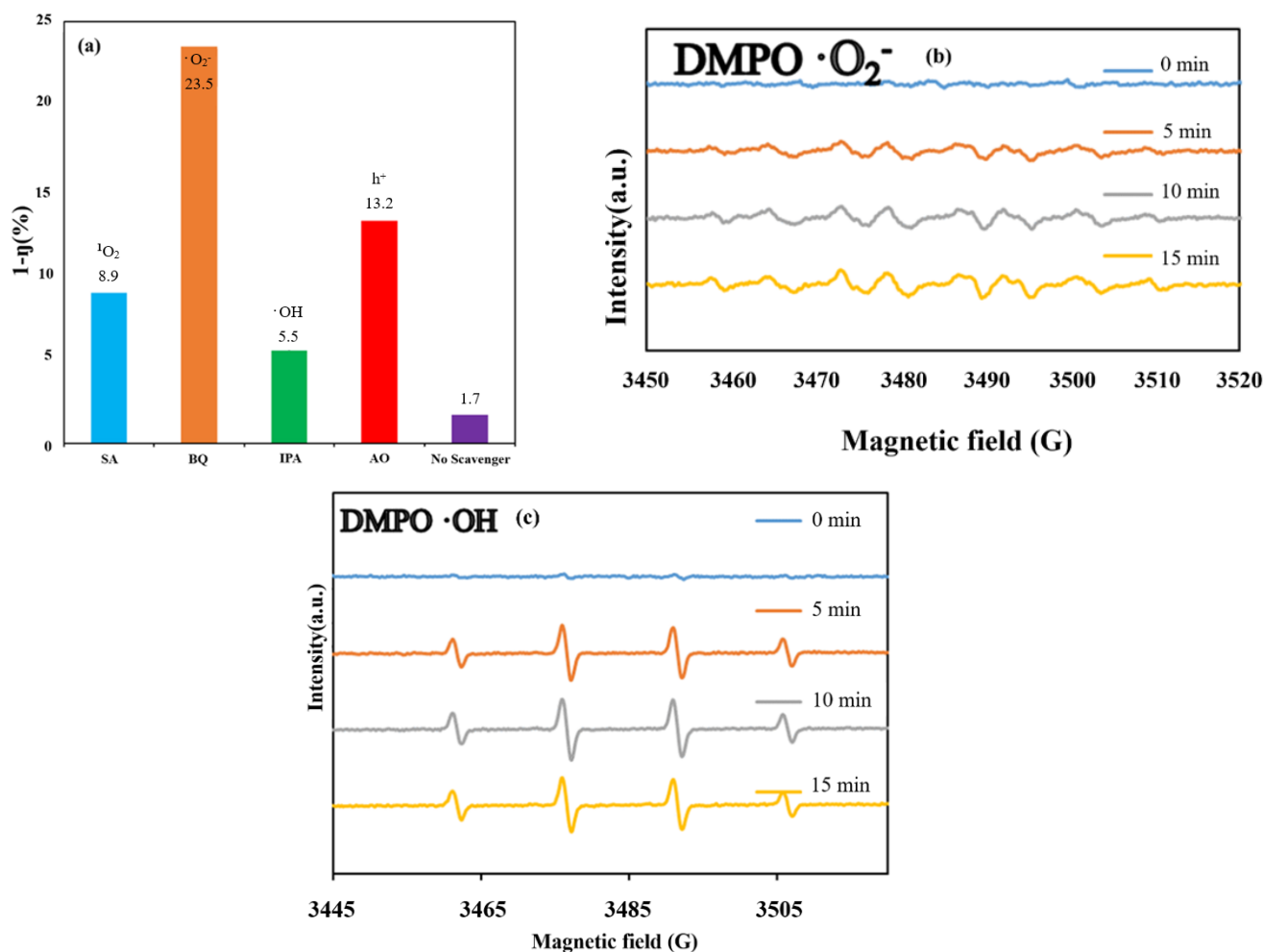


Figure 12. (a) Variations in the dye concentration with the irradiation time on the BiOmCln/BiOpIq/g-C₃N₄-20% photocatalyst prepared under a KCl:KI molar ratio of 1:2, a hydrothermal temperature of 250 °C, and a pH of 4 when using different scavengers (i.e., sodium azide, p-benzoquinone, ammonium oxalate, and isopropanol). Electron paramagnetic resonance spectra for (b) DMPO-•O₂⁻ and (c) DMPO-•OH on the aforementioned catalyst under visible-light irradiation.

EPR spectroscopy can be used to detect the •OH and •O₂⁻ radicals produced through the reactions of photogenerated holes and electrons with H₂O and O₂ during the photocatalytic degradation process [57,58]. We used 5,5-dimethyl-1-pyrroline N-oxide (DMPO) as a free radical scavenger to produce photocatalytic degradation. DMPO when dissolved in an aqueous solution can be used to detect whether a catalyst produces •OH during a photocatalytic reaction. Moreover, DMPO dissolved in methanol solution can be used to identify the production of •O₂⁻ by a catalyst in a photocatalytic reaction.

Figure 12b displays the EPR spectrum of the BC1I2-4-250-g-C₃N₄-20% sample in a solution of DMPO in methanol. The results in the aforementioned figure indicate the absence of any detected EPR signal when the aforementioned sample was in the dark room, and the characteristic •O₂⁻ peak appeared after 5 min of illumination. Thus, the aforementioned catalyst contained the •O₂⁻ active species. Figure 12c depicts the EPR spectrum of the aforementioned sample in an aqueous solution containing DMPO. No EPR signal was observed in the dark room, and a characteristic 1:2:2:1 peak appeared after 5 min of illumination. These results indicate that the aforementioned catalyst contained the •OH active species.

A comparison of the results displayed in Figure 12a–c with the results presented in the literature [2,38] indicated that the EPR signal of •OH was relatively stable and had a more

consistent trend with that of the scavenger method for measuring active species. The EPR signal of $\bullet\text{O}_2^-$ was relatively unstable. Although the EPR signal of $\bullet\text{O}_2^-$ appeared to be weak, $\bullet\text{O}_2^-$ was a dominant active species in the aforementioned photocatalyst [38].

2.3. Schematic of Bandgap Structures of BiOCl/BiOI/g-C₃N₄

Figure 13 depicts a schematic of a hypothetical mechanism of the photocatalytic effect of BiO_mCl_n/BiO_pI_q/g-C₃N₄ in the reduction of CO₂ (Figure 13a) and photocatalytic degradation of a CV aqueous solution dye (Figure 13b). Figure 13a clarifies the mechanism approach, which can optimize the overall CO₂ conversion rate. Through thermodynamic or kinetic control, the selectivity of the whole product can be improved [59]. Figure 13b illustrates the photosensitization and photocatalytic processes of the aforementioned photocatalyst. When irradiating BiO_mCl_n/BiO_pI_q/g-C₃N₄ with light, the electrons in the valence band of g-C₃N₄ are excited and move to the conduction band of g-C₃N₄. These electrons are transported first to the conduction band of BiOCl and then to the conduction band of BiOI. The aforementioned electrons generate $\bullet\text{O}_2^-$ when they react with O₂ during transportation. If these electrons are transferred back to g-C₃N₄, the electron–hole recombination rate can be effectively reduced.

The BiOCl/BiOI/g-C₃N₄ photocatalyst is a three-phase composite material. The experimental results showed that the photocatalytic activity of the derived composite BiOCl/BiOI/g-C₃N₄ exceeded the activity of the individual components of BiOCl/BiOI by about 9.64 times for CO₂ reduction and 3.6 times for photocatalysis degradation of CV. Therefore, there may be a synergistic effect between BiOCl/BiOI and g-C₃N₄. In fact, many researchers have indicated that there is a synergistic effect in a composite material comprising two contacting semiconductors [49,60]. The above effect is ascribed to the effective charge transfer achieved at the interface of the two semiconductors. The described phenomenon may produce the effectiveness of photo-excited electron–hole separation, thereby increasing photocatalytic activity. The charge transfer process is driven by the corresponding relationship of the band potentials. Therefore, a suitable band potential constitutes a prerequisite related to the synergistic effect of the composite photocatalyst.

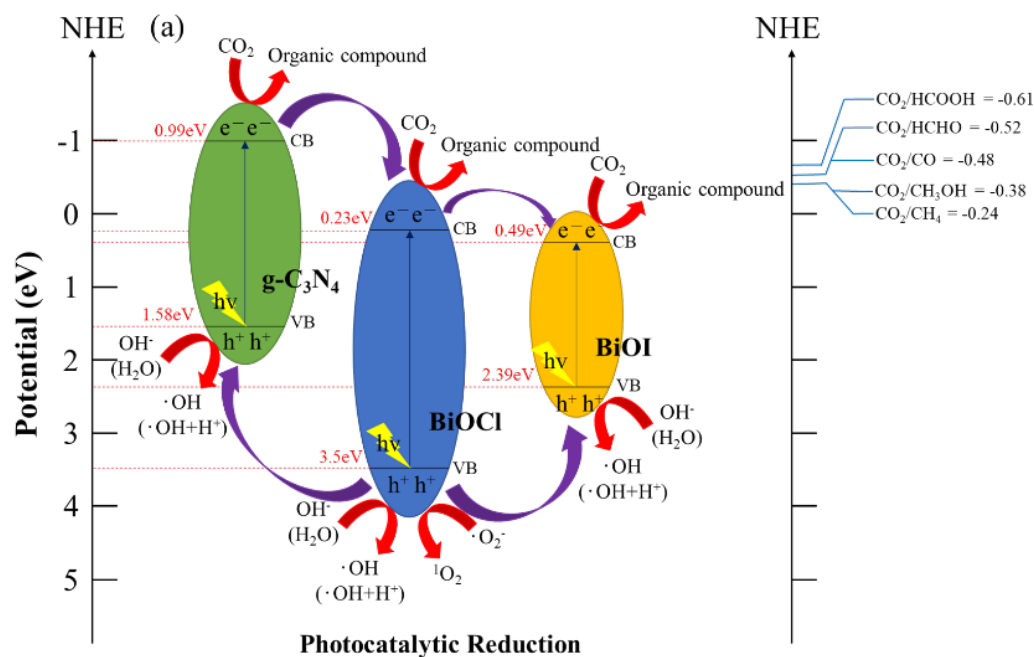


Figure 13. Cont.

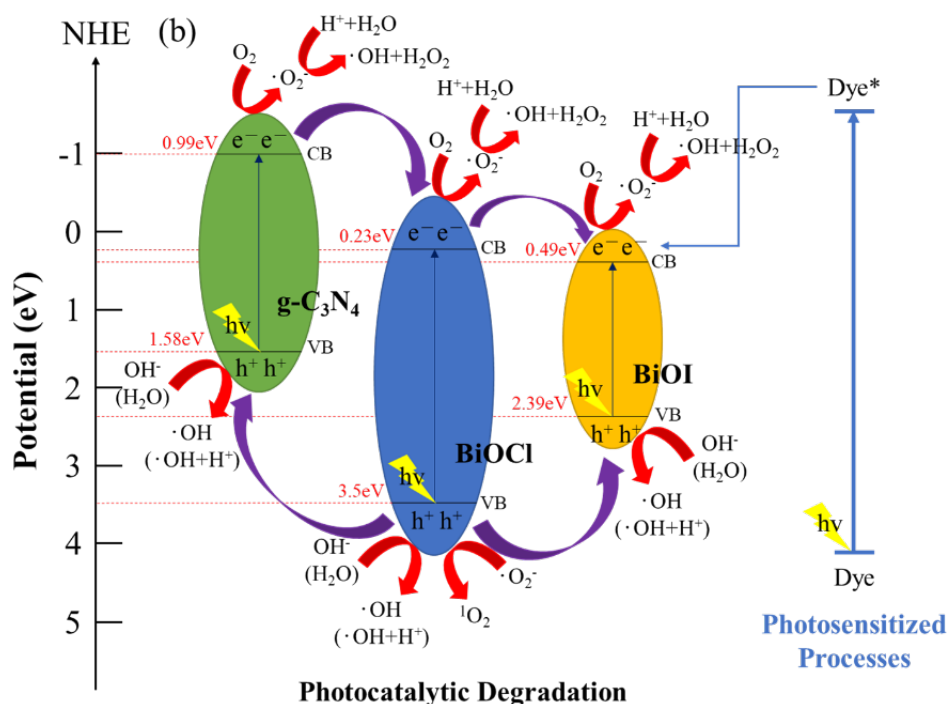


Figure 13. Band structure diagram and possible charge separation processes of the BiOmCln/BiOpIq/g-C₃N₄-20% photocatalyst prepared under a KCl:KI molar ratio of 1:2, a hydrothermal temperature of 250 °C, and a pH of 4 for (a) photocatalytic reduction of CO₂ and (b) photocatalytic degradation of dye.

The prerequisite for decomposing CV dyes is that the electrons in the conduction band of BiOX (X = Cl, I) are transferred to the bulk solution, and react with the aqueous solution to form reactive oxygen species, so the photocatalysis and photosensitization processes can be carried out simultaneously. These photogenerated and photosensitive electrons leaving the material interface, after reaching the bulk solution, interact with the photocatalyst-surface-dwelling oxygen; then, $\bullet\text{O}_2^-$ radicals are generated. The $\bullet\text{O}_2^-$ radicals are very unstable. It quickly reacts with H^+ ions to form hydroxyl radicals. The h^+ holes will also enter the bulk solution after leaving the valence band interface, react with OH^- ions (or H_2O), and generate hydroxyl radicals [61]. The mechanism of $^1\text{O}_2$ generation is also related to $\bullet\text{O}_2^-$. Through the action of cationic substances (including h^+) and superoxide $\bullet\text{O}_2^-$, one electron in $\bullet\text{O}_2^-$ is transferred to the cationic substance to generate $^1\text{O}_2$ active species [62]. Although $^1\text{O}_2$ does not play any important role in CO₂ reduction and CV degradation, we can still see its presence in active species detection experiments.

In the literature about the mechanism of degradation of CV dyes in the presence of photocatalysts by ultraviolet irradiation, it is believed that nitrogen-centered and carbon-centered free radicals are formed first. Then, there is the opportunity for N-dealkylation and disruption of the dye chromophore structure [35,54,60]. In this study, photocatalytic degradation was carried out with more practical visible light as the light source instead of UV irradiation to degrade the hydroxylated compounds of CV. It was confirmed by this study that the intermediates produced by the semiconductor photocatalyst we used under the catalysis of visible-light irradiation were the same as the intermediates produced by irradiation with ultraviolet light in the literature. In this study, it is believed that photosensitization and photocatalysis will proceed simultaneously during the reaction. The generation of $\bullet\text{O}_2^-$ radicals is caused by the reaction of photosensitive and photogenerated electrons e^- on the surface of the photocatalyst. The generation of $\bullet\text{OH}$ radicals is caused by the reaction of h^+ - OH^- (or H_2O) and $\bullet\text{O}_2^-$ - H^+ . From the experiments of active species, we can see that the two main free radical oxidants ($\bullet\text{OH}$ and $\bullet\text{O}_2^-$) in this work are dominated by $\bullet\text{O}_2^-$.

In the electron transportation process, h^+ oxidizes OH^- and H_2O to produce $\bullet OH$. These free radicals further degrade and react with CV dyes, which results in the formation of mineralized products and the CV dyes absorbing light energy for photosensitization reactions to improve the photocatalytic effect. Because of their heterostructures, the prepared ternary nanocomposites possess the characteristics of heterostructures of type II band alignment [22,24]. Therefore, the Z-scheme effect [63] of improving photocatalytic degradation is achieved.

3. Experimental

3.1. Materials

Potassium chloride (KCl), potassium iodide (KI; Katayama, Osaka, Japan), $Bi(NO_3)_3 \cdot 5H_2O$ (Sigma-Aldrich, St. Louis, MO, USA), 2-hydroxybenzoic acid (2-HBA, Katayama, Osaka, Japan), CV dye (TCI), p-benzoquinone (BQ; Alfa Aesar, Ward Hill, MA, USA), ammonium oxalate (AO; Osaka, Japan), sodium azide (SA; Sigma-Aldrich, St. Louis, MO, USA), and isopropanol (IPA; Merck, Rahway, NJ, USA) were used in the absence of further purification. Moreover, sodium hydroxide, reagent-grade nitric acid, and high-performance liquid-chromatography-grade methanol were from Merck.

3.2. Instruments and Analytical Methods

An MAC Science MXP18 instrument (MAC Science Co., Ltd., Tokyo, Japan), was used with $Cu-K\alpha$ radiation at a current of 80 mA and a working voltage of 40 kV to obtain X-ray diffraction (XRD) spectra. A Scinco SA-13.1 spectrophotometer (Scinco Co., Ltd., Seoul, Republic of Korea) was adopted to measure ultraviolet UV-DRS ($k = 300\text{--}800$ nm) spectra at room temperature. A JEOL-2010 microscope (JEOL Ltd., Tokyo, Japan) with an accelerating voltage of 200 kV was used to perform high-resolution transmission electron microscopy (HR-TEM), field emission transmission electron microscopy (TEM), selected-area electron diffraction (SAED), and electron-dispersive X-ray spectroscopy (EDS). A JEOL JSM-7401F (JEOL Ltd., Tokyo, Japan) microscope with an accelerating voltage of 15 kV was adopted to conduct field emission scanning electron microscopy (FE-SEM)–EDS. Photoluminescence (PL) measurements were performed on a Hitachi F-7000 (Hitachi, Ltd., Tokyo, Japan) device. A Micromeritics Gemini (Gemini-V, Micromeritics, USA) automated system was used with the adsorbate being nitrogen gas at liquid nitrogen temperature for measuring the samples' Brunauer–Emmett–Teller (BET) specific surface areas (S_{BET}). An instrument manufactured by ULVAC-PHI (ULVAC PHI INC. Kanagawa, Japan) was adopted to conduct high-resolution X-ray photoelectron spectroscopy (HR-XPS). Finally, an Agilent 5310A frequency counter operating in the X band and a Bruker ER200D spectrometer (Bruker, Karlsruhe, Germany) were used to record the electron paramagnetic resonance (EPR) spectra.

3.3. Synthesis of Different $BiO_mCl_n/BiO_pI_q/g-C_3N_4$ Composites

The method described as follows was used to produce BiO_mCl_n/BiO_pI_q composites. In a 50 mL flask, we mixed 5 mmol $Bi(NO_3)_3 \cdot 5H_2O$ with 5 mL of 4 M HNO_3 . Then, we added 2 M NaOH dropwise to the aforementioned mixture to adjust its pH value to 1, 4, 7, 10, and 13. Subsequently, 3 M KI and 3 M KCl were added into the aforementioned mixture in a ratio of 2:1 or 1:2. We vigorously stirred the resulting solution for 30 min before transferring it into a 30 mL Teflon-lined autoclave, which we heated to 200, 150, or 100 °C over 30 min; then, we maintained the respective temperature for 24 h and finally left it to naturally cool to room temperature. The formulation of the aforementioned reaction parameters is based on the most appropriate operating conditions and intervals summed up by our laboratory for many years of research on hydrothermal methods [1–6]. After it was cooled to room temperature, we filtered the solution to collect the solid precipitate. During filtration, the precipitate was washed with deionized water for other ionic substances to be removed from it. The precipitate was subsequently dried at 60 °C until the next day. Different BiO_mCl_n/BiO_pBr_q composites could be produced according to the reaction

temperature and pH. Table 1 presents our coding of the samples prepared under various reaction temperatures, pH values, and molar ratios.

Melamine was calcined in a muffle furnace under atmospheric conditions to synthesize $g\text{-C}_3\text{N}_4$ powder directly. A total of 5 g of melamine was placed into an alumina crucible with a lid, which was subsequently heated to 520 °C in 4 h at a heating rate of 10 °C/min. After the crucible was cooled to room temperature, the powdered $g\text{-C}_3\text{N}_4$ was obtained.

The method described as follows was used to produce $\text{BiO}_m\text{Cl}_n/\text{BiO}_p\text{I}_q/g\text{-C}_3\text{N}_4$ composites. Binary Bi oxyhalide was composited with materials having different weight percentages of $g\text{-C}_3\text{N}_4$ (10, 20, 30, 40, 50, 60, 70, 80, and 90 wt%). First, $\text{BiO}_m\text{Cl}_n/\text{BiO}_p\text{I}_q$ was dissolved in 10 mL of ethylene glycol to produce solution A. Second, $g\text{-C}_3\text{N}_4$ was dissolved in 10 mL of ethylene glycol to produce solution B. Third, solutions A and B were mixed, stirred for 30 min, autoclaved, and then heated in an oven to 150 °C over 4 h. The total amount of $\text{BiO}_m\text{Cl}_n/\text{BiO}_p\text{I}_q$ and $g\text{-C}_3\text{N}_4$ in each batch was 0.2 g. Subsequently, we filtered the mixture before drying and ground it to obtain $\text{BiO}_m\text{Cl}_n/\text{BiO}_p\text{I}_q/g\text{-C}_3\text{N}_4$.

3.4. Photocatalytic Experiments

3.4.1. Reduction of CO_2

A three-necked flask was charged with 300 mL of an aqueous solution of 1 N NaOH and 0.1 g of photocatalyst. Then, we used a compressed steel cylinder containing CO_2 (99.99%) with a mass flow controller at a delivery rate of 500 mL/min for 1 h to adjust the CO_2 content of the aqueous solution to saturation. Photocatalyst reduction of CO_2 was carried out under a light source. In the process of CO_2 reduction, 1 mL of the gas above the solution was drawn out with a syringe needle every 24 h, and then injected into the GC. The concentration of CH_4 reduced from CO_2 was obtained from GC analysis.

3.4.2. Degradation of Dye

In the conducted photocatalytic experiments, 100 mL of 10 ppm of CV dye was used as the degradation product and 0.05 g of $\text{BiO}_m\text{Cl}_n/\text{BiO}_p\text{I}_q/g\text{-C}_3\text{N}_4$ was used as the photocatalyst. The solution was irradiated under a 15 W visible fluorescent light to produce a photocatalytic reaction. Prior to the beginning of the photocatalytic reaction, the solution was stirred in a dark room with a magnet for 30 min. After we confirmed the absorption–desorption equilibrium of the dye and catalyst at room temperature, stirring was continued and degradation occurred under irradiation with visible light. A 5 mL sample of the solution was obtained at different intervals (4, 8, 12, 24, 48, 72, and 96 h) and centrifuged at 4000 rpm for 30 min after which it became clear. The concentration of the CV aqueous solution was measured using a Scinco S-3000 spectrophotometer (Photo Diode Array UV–visible, UV–vis PDA). Absorption bands of the CV dye were located at 591.

4. Conclusions

In this study, the $\text{BiO}_m\text{Cl}_n/\text{BiO}_p\text{I}_q/g\text{-C}_3\text{N}_4$ photocatalyst was successfully produced using a high-pressure hydrothermal method, as verified by XRD results. The DRS results indicated that the addition of $g\text{-C}_3\text{N}_4$ effectively reduced the bandgap value of the aforementioned photocatalyst and made it easier for the photocatalyst to absorb visible light. The TEM analysis indicated that $g\text{-C}_3\text{N}_4$ was successfully composited with $\text{BiO}_m\text{Cl}_n/\text{BiO}_p\text{I}_q$. The BET analysis indicated that the adsorption–desorption isotherm of $\text{BiO}_m\text{Cl}_n/\text{BiO}_p\text{I}_q/g\text{-C}_3\text{N}_4$ was in agreement with those of mesoporous catalysts. In an analysis of the degradation rate of the prepared catalyst with and without $g\text{-C}_3\text{N}_4$, the addition of $g\text{-C}_3\text{N}_4$ increased the degradation rate of the photocatalyst by up to three times. In reuse tests, $\text{BiO}_m\text{Cl}_n/\text{BiO}_p\text{I}_q/g\text{-C}_3\text{N}_4$ had a degradation efficiency of 90.5% after its third use, which indicated that this catalyst was recyclable. Moreover, XRD results indicated that the aforementioned catalyst had the same crystal phase even after being used multiple times, which indicated that this catalyst had high stability. The conversion efficiency of CO_2 reduction to CH_4 of $\text{BiO}_m\text{Cl}_n/\text{BiO}_p\text{I}_q$ of $4.09 \mu\text{mol g}^{-1}$ can be increased to $39.43 \mu\text{mol g}^{-1}$ by compositing with $g\text{-C}_3\text{N}_4$. It had an approximately 9.64 times improvement. The

photodegradation rate constant for CV of BiO_mCl_n/BiO_pI_q can be increased to 0.2456 by complexation with g-C₃N₄. It had an approximately 3.6 times improvement.

Supplementary Materials: The following supporting information can be downloaded at: <https://www.mdpi.com/article/10.3390/catal13030522/s1>, Figure S1: XRD patterns of the BiO_mCl_n/BiO_pI_q samples prepared under a KCl:KI molar ratio of 1:2, a pH of 1–13, a reaction time of 12 h, and a hydrothermal temperature of 100 °C; Figure S2: XRD patterns of the BiO_mCl_n/BiO_pI_q samples prepared under a KCl:KI molar ratio of 1:2, a pH of 1–13, a reaction time of 12 h, and a hydrothermal temperature of 150 °C; Figure S3: XRD patterns of the BiO_mCl_n/BiO_pI_q samples prepared under a KCl:KI molar ratio of 1:2, a pH of 1–13, a reaction time of 12 h, and a hydrothermal temperature of 200 °C; Figure S4: XRD patterns of the BiO_mCl_n/BiO_pI_q samples prepared under a KCl:KI molar ratio of 1:2, a pH of 1–13, a reaction time of 12 h, and a hydrothermal temperature of 250 °C; Figure S5: XRD patterns of the BiO_mCl_n/BiO_pI_q samples prepared under a KCl:KI molar ratio of 2:1, a pH of 1–13, a reaction time of 12 h, and a hydrothermal temperature of 100 °C; Figure S6: XRD patterns of the BiO_mCl_n/BiO_pI_q samples prepared under a KCl:KI molar ratio of 2:1, a pH of 1–13, a reaction time of 12 h, and a hydrothermal temperature of 150 °C; Figure S7: XRD patterns of the BiO_mCl_n/BiO_pI_q samples prepared under a KCl:KI molar ratio of 2:1, a pH of 1–13, a reaction time of 12 h, and a hydrothermal temperature of 200 °C; Figure S8: XRD patterns of the BiO_mCl_n/BiO_pI_q samples prepared under a KCl:KI molar ratio of 2:1, a pH of 1–13, a reaction time of 12 h, and a hydrothermal temperature of 250 °C; Figure S9: Scanning electron microscopy images of the BiO_mCl_n/BiO_pI_q/g-C₃N₄-20% samples prepared using the hydrothermal autoclave method under a KCl:KI molar ratio of 1:2, different pH values, a reaction time of 12 h, and a hydrothermal temperature of 250 °C; Figure S10: UV–vis absorption spectra of the BiO_mCl_n/BiO_pI_q photocatalysts prepared under a KCl:KI molar ratio of 1:2, a hydrothermal temperature of 250 °C, and various pH values; Figure S11: UV–vis absorption spectra of the BiO_mCl_n/BiO_pI_q photocatalysts prepared under a KCl:KI molar ratio of 1:2, a pH of 1–13, and a hydrothermal temperature of 250 °C; Table S1: Chemical and physical properties of the BC1I2-4-250-g-C₃N₄-20% sample.

Author Contributions: Conceptualization, C.-C.C.; methodology, S.-H.C. and F.-Y.L.; software, H.-L.W.; validation, S.-H.C. and Y.-Y.L.; formal analysis, H.-L.W.; investigation, J.-M.J.; resources, J.-M.J.; data curation, H.-L.W. and J.-H.L.; writing—original draft preparation, Y.-M.D. and W.-T.W.; writing—review and editing, C.-C.C., Y.-M.D., W.-T.W. and Y.-Y.L.; visualization, S.-H.C.; supervision, C.-C.C.; project administration, Y.-M.D.; funding acquisition, C.-C.C. All authors have read and agreed to the published version of the manuscript.

Funding: This research was funded by the Ministry of Science and Technology (Grant No.: MOST-109-2113-M-142 -001), Taiwan.

Data Availability Statement: The data is included in the article or Supplementary Materials.

Acknowledgments: We thank the Ministry of Science and Technology of Taiwan (MOST-109-2113-M-142 -001) for financially supporting this study, and thank the Instrumentation Center of Chung Hsing University, Taiwan (MOST110-2731-M-005-001, EM022400, EPR000000400); Instrumentation Center at National Tsing Hua University, Taiwan (MOST110-2731-M-007-001, ESCA00002603); Precious Instrument Utilization Center at National Central University, Taiwan (MOST110-2731-M-008-001, ESCA00001005) for utilization of precious instruments.

Conflicts of Interest: The authors declare no conflict of interest.

References

1. Lee, D.H.; Porta, M.; Jacobs, D.R.; Vandenberg, L.N., Jr. Chlorinated persistent organic pollutants, obesity, and type 2 diabetes. *Endocr. Rev.* **2014**, *35*, 557–601. [[CrossRef](#)] [[PubMed](#)]
2. Chen, H.L.; Liu, F.Y.; Xiao, X.; Hu, J.; Gao, B.; Zou, D.; Chen, C.C. Visible-light-driven photocatalysis of carbon dioxide and organic pollutants by MFeO₂ (M = Li, Na, or K). *J. Colloid Interface Sci.* **2021**, *601*, 758–772. [[CrossRef](#)] [[PubMed](#)]
3. Liu, F.Y.; Dai, Y.M.; Chen, F.H.; Chen, C.C. Lead bismuth oxybromide/graphene oxide: Synthesis, characterization, and photocatalytic activity for removal of carbon dioxide, crystal violet dye, and 2-hydroxybenzoic acid. *J. Colloid Interface Sci.* **2020**, *562*, 112–124. [[CrossRef](#)] [[PubMed](#)]
4. He, J.; Liu, J.; Hou, Y.; Wang, Y.; Yang, S.; Yang, H.G. Surface chelation of cesium halide perovskite by dithiocarbamate for efficient and stable solar cells. *Nat. Commun.* **2020**, *11*, 4237. [[CrossRef](#)] [[PubMed](#)]
5. Ramirez, D.; Velilla, E.; Montoya, J.F.; Jaramillo, F. Mitigating scalability issues of perovskite photovoltaic technology through a p-i-n meso-superstructured solar cell architecture. *Sol. Energy Mater. Sol. Cells* **2019**, *195*, 191–197. [[CrossRef](#)]

6. Zheng, J.; Lei, Z. Incorporation of CoO nanoparticles in 3D marigold flower-like hierarchical architecture MnCo₂O₄ for highly boosting solar light photo-oxidation and reduction ability. *Appl. Catal. B Environ.* **2018**, *237*, 1–8. [[CrossRef](#)]
7. Yin, R.; Li, Y.; Zhong, K.; Yao, H.; Zhang, Y.; Lai, K. Multifunctional property exploration: Bi₄O₅I₂ with high visible light photocatalytic performance and a large nonlinear optical effect. *RSC Adv.* **2019**, *9*, 4539–4544. [[CrossRef](#)]
8. Chang, C.; Zhu, L.; Wang, S.; Chu, X.; Yue, L. Novel mesoporous graphite carbon nitride/BiOI heterojunction for enhancing photocatalytic performance under visible-light irradiation. *Appl. Mater. Interfaces* **2014**, *6*, 5083–5093. [[CrossRef](#)]
9. Ye, L.; Su, Y.; Jin, X.; Xie, H.; Zhang, C. Recent advances in BiOX (X = Cl, Br and I) photocatalysts: Synthesis, modification, facet effects and mechanisms. *Environ. Sci. Nano* **2014**, *1*, 90–112. [[CrossRef](#)]
10. Bai, Y.; Wang, P.Q.; Liu, J.Y.; Liu, X.J. Enhanced photocatalytic performance of direct Z-scheme BiOCl-g-C₃N₄ photocatalysts. *RSC Adv.* **2014**, *4*, 19456. [[CrossRef](#)]
11. Bu, Y.; Xu, J.; Li, Y.; Liu, Q.; Zhang, X. Enhanced photocatalytic activity of BiOI under visible light irradiation by the modification of MoS₂. *RSC Adv.* **2017**, *7*, 42398–42406. [[CrossRef](#)]
12. Bhachu, D.S.; Moniz, S.J.A.; Sathasivam, S.; Scanlon, D.O.; Walsh, A.; Bawaked, S.M.; Mokhtar, M.; Obaid, A.Y.; Parkin, I.P.; Tang, J.; et al. Bismuth oxyhalides: Synthesis, structure and photoelectrochemical activity. *Chem. Sci.* **2016**, *7*, 4832–4841. [[CrossRef](#)]
13. Singh, M.; Kumar, A.; Krishnan, V. Influence of different bismuth oxyhalides on the photocatalytic activity of graphitic carbon nitride: A comparative study under natural sunlight. *Mater. Adv.* **2020**, *1*, 1262–1272. [[CrossRef](#)]
14. Zheng, M.; Ma, X.; Hu, J.; Zhang, X.; Duan, W. Novel recyclable BiOBr/Fe₃O₄/RGO composites with remarkable visible-light photocatalytic activity. *RSC Adv.* **2020**, *10*, 19961–19973. [[CrossRef](#)]
15. Wang, X.; Maeda, K.; Thomas, A.; Takanabe, K.; Xin, G.; Carlsson, J.; Domen, K.; Antonietti, M. A metal-free polymeric photocatalyst for hydrogen production from water under visible light. *Nat. Mater.* **2008**, *8*, 76–80. [[CrossRef](#)]
16. Jiang, D.; Chen, L.; Zhu, J.; Chen, M.; Shi, W.; Xie, J. Novel p-n heterojunction photocatalyst constructed by porous graphite-like C₃N₄ and nanostructured BiOI: Facile synthesis and enhanced photocatalytic activity. *Dalton Trans.* **2013**, *42*, 15726–15734. [[CrossRef](#)]
17. Zhao, Z.; Sun, Y.; Dong, F. Graphitic carbon nitride based nano composites: A review. *Nanoscale* **2015**, *7*, 15–37. [[CrossRef](#)]
18. Yang, C.T.; Lee, W.W.; Lin, H.P.; Dai, Y.M.; Chi, H.T.; Chen, C.C. A novel heterojunction photocatalyst, Bi₂SiO₅/g-C₃N₄ synthesis, characterization, photocatalytic activity, and mechanism. *RSC Adv.* **2016**, *6*, 40664. [[CrossRef](#)]
19. Lin, H.P.; Chen, C.C.; Lee, W.W.; Lai, Y.Y.; Chen, J.Y.; Chen, Y.Q.; Fu, J.Y. Synthesis of a SrFeO_{3-x}/g-C₃N₄ heterojunction with improved visible-light photocatalytic activities in chloramphenicol and crystal violet degradation. *RSC Adv.* **2016**, *6*, 2323. [[CrossRef](#)]
20. Chou, S.Y.; Chen, C.C.; Dai, Y.M.; Lin, J.H.; Lee, W.W. Novel synthesis of bismuth oxyiodide/graphitic carbon nitride nanocomposites with enhanced visible-light photocatalytic activity. *RSC Adv.* **2016**, *6*, 33478–33491. [[CrossRef](#)]
21. Wang, B.; Di, J.; Liu, G.; Yin, S.; Xia, J.; Zhang, Q.; Li, H. Novel mesoporous graphitic carbon nitride modified PbBiO₂Br porous microspheres with enhanced photocatalytic performance. *J. Colloid Interface Sci.* **2017**, *507*, 310–322. [[CrossRef](#)] [[PubMed](#)]
22. Lee, A.H.; Wang, Y.C.; Chen, C.C. Composite photocatalyst, tetragonal lead bismuth oxyiodide/bismuth oxyiodide/graphitic carbon nitride synthesis, characterization, and photocatalytic activity. *J. Colloid Interface Sci.* **2019**, *533*, 319–332. [[CrossRef](#)] [[PubMed](#)]
23. Wang, Y.C.; Lee, A.H.; Chen, C.C. Perovskite-like photocatalyst, PbBiO₂/BrPbO/g-C₃N₄ synthesis, characterization, and visible-light-driven photocatalytic activity. *J. Taiwan Inst. Chem. Eng.* **2018**, *93*, 315–328. [[CrossRef](#)]
24. Li, Z.; Feng, J.; Yan, S.; Zou, Z. Solar fuel production: Strategies and new opportunities with nanostructures. *Nano Today* **2015**, *10*, 468–486. [[CrossRef](#)]
25. Huang, H.; Pradhan, B.; Hofkens, J.; Roelofs, M.B.J.; Steele, J.A. Solar-driven metal halide perovskite photocatalysis: Design, stability, and performance. *Energy Lett.* **2020**, *5*, 1107–1123. [[CrossRef](#)]
26. Chen, S.; Huang, D.; Cheng, M.; Lei, L.; Chen, Y.; Zhou, C.; Deng, R.; Li, B. Surface and interface engineering of two-dimensional bismuth-based photocatalysts for ambient molecule activation. *J. Mater. Chem. A* **2021**, *9*, 196–233. [[CrossRef](#)]
27. Wang, B.; Zhao, J.; Chen, H.; Weng, Y.X.; Tang, H.; Chen, Z.; Zhu, W.; She, Y.; Xia, J.; Li, H. Unique Z-scheme carbonized polymer dots/Bi₄O₅Br₂ hybrids for efficiently boosting photocatalytic CO₂ reduction. *Appl. Catal. B Environ.* **2021**, *293*, 120128. [[CrossRef](#)]
28. Xu, Q.; Zhang, L.; Cheng, B.; Fan, J.; Yu, J. S-scheme heterojunction photocatalyst. *Chem* **2020**, *6*, 1543–1559. [[CrossRef](#)]
29. Wang, Y.; Wang, K.; Wang, J.; Wu, X.; Zhang, G. Sb₂WO₆/BiOBr 2D nanocomposite S-scheme photocatalyst for NO removal. *J. Mater. Sci. Technol.* **2020**, *56*, 236–243. [[CrossRef](#)]
30. Chen, C.C.; Fu, J.Y.; Chang, J.L.; Huang, S.T.; Yeh, T.W.; Huang, J.T.; Huang, P.H.; Liu, F.Y.; Chen, L.W. Bismuth oxyfluoride/bismuth oxyiodide nanocomposites enhance visible-light-driven photocatalytic activity. *J. Colloid Interface Sci.* **2018**, *532*, 375–386. [[CrossRef](#)]
31. Chou, Y.C.; Lin, Y.Y.; Lu, C.S.; Liu, F.Y.; Lin, J.H.; Chen, F.H.; Chen, C.C.; Wu, W.T. Controlled hydrothermal synthesis of BiO_xCl_y/BiO_mBr_n/g-C₃N₄ composites exhibiting visible-light photocatalytic activity. *J. Environ. Manag.* **2021**, *297*, 113256. [[CrossRef](#)]
32. Siao, C.W.; Lee, W.L.W.; Dai, Y.M.; Chung, W.H.; Hung, J.T.; Hung, P.H.; Lin, W.Y.; Chen, C.C. BiO_xCl_y/BiO_mBr_n/BiO_pI_q/GO quaternary composites syntheses and application of visible-light-driven photocatalytic activities. *J. Colloid Interface Sci.* **2019**, *544*, 25–36. [[CrossRef](#)]

33. Wang, X.J.; Wang, Q.; Li, F.T.; Yang, W.Y.; Zhao, Y.; Hao, Y.J.; Liu, S.J. Novel BiOCl–C₃N₄ heterojunction photocatalysts: In situ preparation via an ionic-liquid-assisted solvent-thermal route and their visible-light photocatalytic activities. *Chem. Eng. J.* **2013**, *234*, 361–371. [[CrossRef](#)]
34. Ye, L.; Liu, J.; Jiang, Z.; Peng, T.; Zan, L. Facets coupling of BiOBr-g-C₃N₄ composite photocatalyst for enhanced visible-light-driven photocatalytic activity. *Appl. Catal. B Environ.* **2013**, *142–143*, 1–7. [[CrossRef](#)]
35. Jiang, Y.R.; Lin, H.P.; Chung, W.H.; Dai, Y.M.; Lin, W.Y.; Chen, C.C. Controlled hydrothermal synthesis of BiO_xCl_y/BiO_mI_n composites exhibiting visible-light photocatalytic degradation of crystal violet. *J. Hazard. Mater.* **2015**, *283*, 787–805. [[CrossRef](#)]
36. Lee, W.W.; Lu, C.S.; Chuang, C.W.; Chen, Y.J.; Fu, J.Y.; Siao, C.W.; Chen, C.C. Synthesis of bismuth oxyiodides and their composites: Characterization, photocatalytic activity, and degradation mechanisms. *RSC Adv.* **2015**, *5*, 23450–23463. [[CrossRef](#)]
37. Xiao, X.; Liu, C.; Hu, R.; Zuo, X.; Nan, J.; Li, L.; Wang, L. Oxygen-rich bismuth oxyhalides: Generalized one-pot synthesis, band structures and visible-light photocatalytic properties. *J. Mater. Chem.* **2012**, *22*, 22840–22843. [[CrossRef](#)]
38. Chen, C.C.; Chen, T.T.; Shaya, J.; Wu, C.L.; Lu, C.S. Bi₁₂SiO₂₀/g-C₃N₄ heterojunctions: Synthesis, characterization, photocatalytic activity for organic pollutant degradation, and mechanism. *J. Taiwan Inst. Chem. Eng.* **2021**, *123*, 228–244. [[CrossRef](#)]
39. Li, T.B.; Chen, G.; Zhou, C.; Shen, Z.Y.; Jin, R.C.; Sun, J.X. New photocatalyst BiOCl/BiOI composites with highly enhanced visible light photocatalytic performances. *Dalton Trans.* **2011**, *40*, 6751–6758. [[CrossRef](#)]
40. Song, L.; Zhang, S.; Wei, Q. Porous BiOI sonocatalysts: Hydrothermal synthesis, characterization, sonocatalytic, and kinetic properties. *Ind. Eng. Chem. Res.* **2012**, *51*, 1193–1197. [[CrossRef](#)]
41. Zhu, L.P.; Liao, G.H.; Bing, N.C.; Wang, L.L.; Yang, Y.; Xie, H.Y. Self-assembled 3D BiOCl architectures: Tunable synthesis and characterization. *CrystEngComm* **2010**, *2*, 3791–3796. [[CrossRef](#)]
42. Sing, K.S.W.; Everett, D.H.; Haul, R.A.W.; Moscou, L.; Pierotti, R.A.; Rouquerol, J.; Siemieniewska, T. Reporting physisorption data for gas/solid systems with special reference to the determination of surface area and porosity (Recommendations 1984). *Pure Appl. Chem.* **1985**, *57*, 603–619. [[CrossRef](#)]
43. Tian, Z.; Yang, X.; Chen, Y.; Huang, H.; Hu, J.; Wen, B. Fabrication of alveolate g-C₃N₄ with nitrogen vacancies via cobalt introduction for efficient photocatalytic hydrogen evolution. *Int. J. Hydrog. Energy* **2020**, *45*, 24792–24806. [[CrossRef](#)]
44. Xu, S.; Carter, E.A. Theoretical insights into heterogeneous (photo) electrochemical CO₂ reduction. *Chem. Rev.* **2019**, *119*, 6631–6669. [[CrossRef](#)] [[PubMed](#)]
45. Huang, J.; Mensi, M.; Oveisi, E.; Mantella, V.; Buonsanti, R. Structural sensitivities in bimetallic catalysts for electrochemical CO₂ reduction revealed by Ag–Cu nanodimers. *J. Am. Chem. Soc.* **2019**, *141*, 2490–2499. [[CrossRef](#)]
46. Parvanian, A.M.; Sadeghi, N.; Rafiee, A.; Shearer, C.J.; Jafarian, M. Application of porous materials for CO₂ reutilization: A review. *Energies* **2022**, *15*, 63. [[CrossRef](#)]
47. Xie, C.; Niu, Z.; Kim, D.; Li, M.; Yang, P. Surface and interface control in nanoparticle catalysis. *Chem. Rev.* **2020**, *120*, 1184–1249. [[CrossRef](#)]
48. Gao, C.; Low, J.; Long, R.; Kong, T.; Zhu, J.; Xiong, Y. Heterogeneous single-atom photocatalysts: Fundamentals and applications. *Chem. Rev.* **2020**, *120*, 12175–12216. [[CrossRef](#)]
49. Wei, X.; Akbar, M.U.; Raza, A.; Li, G. A review on bismuth oxyhalide based materials for photocatalysis. *Nanoscale Adv.* **2021**, *3*, 3353–3372. [[CrossRef](#)]
50. Wang, L.; Chen, W.; Zhang, D.; Du, Y.; Amal, R.; Qiao, S.; Wu, J.; Yin, Z. Surface strategies for catalytic CO₂ reduction: From two-dimensional materials to nanoclusters to single atoms. *Chem. Soc. Rev.* **2019**, *48*, 5310–5349. [[CrossRef](#)]
51. Yang, L.; Peng, Y.; Luo, X.; Dan, Y.; Ye, J.; Zhou, Y.; Zou, Z. Beyond C₃N₄ π-conjugated metal-free polymeric semiconductors for photocatalytic chemical transformations. *Chem. Soc. Rev.* **2021**, *50*, 2147–2172. [[CrossRef](#)]
52. Siao, C.W.; Chen, H.L.; Chen, L.W.; Chang, J.L.; Yeh, T.W.; Chen, C.C. Controlled hydrothermal synthesis of bismuth oxychloride-bismuth oxybromide-bismuth oxyiodide composites exhibiting visible-light photocatalytic degradation of 2-hydroxybenzoic acid and crystal violet. *J. Colloid Interface Sci.* **2018**, *526*, 322–336. [[CrossRef](#)]
53. Li, K.L.; Lee, W.W.; Lu, C.S.; Dai, Y.M.; Chou, S.Y.; Chen, H.L.; Lin, H.P.; Chen, C.C. Synthesis of BiOBr, Bi₃O₄Br, and Bi₁₂O₁₇Br₂ by controlled hydrothermal method and their photocatalytic properties. *J. Taiwan Inst. Chem. Eng.* **2014**, *45*, 2688–2697. [[CrossRef](#)]
54. Jiang, Y.R.; Chou, S.Y.; Chang, J.L.; Huang, S.T.; Lin, H.P.; Chen, C.C. Hydrothermal synthesis of bismuth oxybromide–bismuth oxyiodide composites with high visible light photocatalytic performance for the degradation of CV and phenol. *RSC Adv.* **2015**, *5*, 30851–30860. [[CrossRef](#)]
55. Liao, Y.H.B.; Wang, J.X.; Lin, J.S.; Chung, W.H.; Lin, W.Y.; Chen, C.C. Synthesis, photocatalytic activities and degradation mechanism of Bi₂WO₆ toward crystal violet dye. *Catal. Today* **2011**, *174*, 148–159. [[CrossRef](#)]
56. Oppong, S.O.B.; Opoku, F.; Govender, P.P. Remarkable Enhancement of Eu–TiO₂–GO Composite for Photodegradation of Indigo Carmine: A Design Method Based on Computational and Experimental Perspectives. *Catal. Lett.* **2020**, *151*, 1111–1126. [[CrossRef](#)]
57. Chen, L.W.; Chen, H.L.; Lu, C.S.; Huang, S.T.; Yeh, T.W.; Chen, C.C. Preparation of perovskite-like PbBiO₂I/g-C₃N₄ exhibiting visible-light-driven activity. *Catal. Today* **2021**, *375*, 472–483. [[CrossRef](#)]
58. Dimitrijevic, N.M.; Vijayan, B.K.; Poluektov, O.G.; Rajh, T.; Gray, K.A.; He, H.; Zapol, P. Role of water and carbonates in photocatalytic transformation of CO₂ to CH₄ on titania. *J. Am. Chem. Soc.* **2011**, *133*, 3964–3971. [[CrossRef](#)]
59. Gandhi, R.; Moses, A.; Sundar Baral, S. Fundamental study of the photocatalytic reduction of CO₂: A short review of thermodynamics, kinetics and mechanisms. *Chem. Process Eng.* **2022**, *43*, 223–228.

60. Li, H.; Zhou, Y.; Tu, W.; Ye, J.; Zou, Z. State-of-the-art progress in diverse heterostructured photocatalysts toward promoting photocatalytic performance. *Adv. Funct. Mater.* **2015**, *25*, 998–1013. [[CrossRef](#)]
61. Fan, H.J.; Lu, C.S.; Lee, W.L.; Chiou, M.R.; Chen, C.C. Mechanistic pathways differences between P25-TiO₂ and Pt-TiO₂ mediated CV photodegradation. *J. Hazard. Mater.* **2011**, *185*, 227–235. [[CrossRef](#)] [[PubMed](#)]
62. He, W.; Jia, H.; Wamer, W.G.; Zheng, Z.; Li, P.; Callahan, J.H.; Yin, J.-J. Predicting and identifying reactive oxygen species and electrons for photocatalytic metal sulfide micro–nano structures. *J. Catal.* **2014**, *320*, 97–105. [[CrossRef](#)]
63. Wang, Y.; Huang, H.; Zhang, Z.; Wang, C.; Yang, Y.; Li, Q.; Xu, D. Lead-free perovskite Cs₂AgBiBr₆@g-C₃N₄ Z-scheme system for improving CH₄ production in photocatalytic CO₂ reduction. *Appl. Catal. B Environ.* **2021**, *282*, 119570. [[CrossRef](#)]

Disclaimer/Publisher's Note: The statements, opinions and data contained in all publications are solely those of the individual author(s) and contributor(s) and not of MDPI and/or the editor(s). MDPI and/or the editor(s) disclaim responsibility for any injury to people or property resulting from any ideas, methods, instructions or products referred to in the content.